Journal of Nanobiotechnology

RESEARCH Open Access

Selenium nanoparticles ameliorate lumbar disc degeneration by restoring GPX1-mediated redox homeostasis and mitochondrial function of nucleus pulposus cells

Wei He[1,2†], Xin Tian[1,2†], Quan Zhou[1,2†], Jiaheng Lv[1,2], Yangfeng Li[1,2], Chenyang Jin[2,3], Hao Liu[1], Huiling Yang[1,2], Yong Xu[1,2*], Fan He[1,2*] and Tao Liu[1*]

Abstract

Intervertebral disc degeneration (IVDD) is a prevalent musculoskeletal disorder that involves the excessive accumulation of reactive oxygen species (ROS), resulting in mitochondrial dysfunction and matrix metabolism imbalance in nucleus pulposus cells (NPCs). Selenium, an indispensable trace element, plays a crucial role in maintaining mitochondrial redox homeostasis by being incorporated into antioxidant selenoproteins as selenocysteine. In this study, we employed a straightforward synthesis method to produce selenium nanoparticles (SeNPs) with consistent size and distribution, and evaluated their potential protective effects in ameliorating IVDD. In a simulated inflammatory environment induced by interleukin-1beta (IL-1β) in vitro, SeNPs demonstrated a protective effect on the matrix synthesis capacity of NPCs through the up-regulation of aggrecan and type II collagen, while concurrently suppressing the expression of matrix degradation enzymes including MMP13 and ADAMTS5. Additionally, SeNPs preserved mitochondrial integrity and restored impaired mitochondrial energy metabolism by activating glutathione peroxidase1 (GPX1) to rebalance redox homeostasis. In a rat lumbar disc model induced by puncture, the local administration of SeNPs preserved the hydration of nucleus pulposus tissue, promoted matrix deposition, and effectively mitigated the progression of IVDD. Our results indicate that the enhancement of GPX1 by SeNPs may offer a promising therapeutic approach for IVDD by restoring mitochondrial function and redox homeostasis.

†Wei He, Xin Tian and Quan Zhou contributed equally to this work.

*Correspondence:
Yong Xu
yxu1615@suda.edu.cn
Fan He
fanhe@suda.edu.cn
Tao Liu
liutao8250@suda.edu.cn

Full list of author information is available at the end of the article

Keywords Intervertebral disc degeneration, Nucleus pulposus, Selenium nanoparticles, GPX1, Extracellular matrix, Mitochondrial homeostasis

Introduction

Low back pain (LBP) is one of the most common musculoskeletal disorders that is a leading cause of disability in the aging population worldwide, not only affecting the quality of patients' lives but also imposing a substantial burden on the social economy [1]. Although the pathogenesis of LBP is intricate and multifactorial, intervertebral disc degeneration (IVDD) has been considered as the primary contributor to LBP. Currently conservative treatments for IVDD can only relieve symptoms, including bed rest, physiotherapy, and drug therapy (e.g. nonsteroidal anti-inflammatory drugs) [2]. However, for late-stage IVDD, surgical interventions are adpoted to remove the degenerated discs but cause various side effects, such as immobilization and loss of spine function [3]. Neither of the two types of treatments are satisfactory because of their failure to restore the physiological structure of discs with normal mechanical functions.

The intervertebral disc (IVD) comprises three distinct tissue zones: the central nucleus pulposus (NP), surrounding peripheral lamellar annulus fibrosus, and two cartilaginous endplates, providing support for load distribution and spinal movement facilitation [4]. Due to the avascular structure, the IVD exhibits a limited capacity for self-repair and is susceptibility to degeneration [5]. Aggrecan (ACAN) and sulfated glycosaminoglycans (GAGs) are the most important components in the extracellular matrix of nucleus pulposus, providing shock absorber function to maintain the IVD mechanical stability. It is believed that the degeneration originates in the NP tissue, which comprises nucleus pulposus cells (NPCs) and proteoglycan-rich matrix contents [6]. During the degeneration process, NPCs undergo phenotypic changes and the cell viability diminishes, along with a significant reduction in hydration due to a loss of proteoglycan content. The progressive loss of gelatinous extracellular matrix (ECM) results in inflammation-induced tissue fibrosis, disruption of the hypoxic environment, ingrowth of nerves and blood vessels, and eventually disc herniation [7].

There is growing body of evidence indicating that oxidative stress is the primary trigger for the onset of IVDD. Oxidative stress occurs as a result of an imbalance between the generation and detoxification of reactive oxygen species (ROS), which are a class of highly active molecules containing oxygen, including singlet oxygen ($^1O_2$), superoxide ($O_2{\bullet}^-$), hydroxyl radical (•OH), and hydrogen peroxide (H_2O_2) [8]. Mitochondria constitute the main source of ROS, which are generated by electron leakage in the mitochondrial respiratory chain and other mitochondrion-located proteins. Excessive ROS production can lead to oxidative damage to crucial cellular components such as lipids, DNA, and proteins, resulting in the dysfunction of the mitochondrial energy metabolism, including insufficient adenosine triphosphate (ATP) production and increased permeability of the mitochondrial membrane [9]. Hartman et al. reported that, compared with those in young and healthy IVDs, aged and degenerated NPCs exhibit a significant reduction in the number of mitochondria, membrane potential, glycolytic capacity, and nonglucose-dependent respiration, in agreement with the age-related decrease in matrix synthesis [10]. This impairment of mitochondrial function eventually leads to programmed cell death and IVDD exacerbation [11].

Intracellular antioxidant enzymes, including superoxide dismutase (SOD), catalase (CAT), and glutathione peroxidases (GPXs), and nonenzymatic antioxidants constitute the system of protection against oxidative damage. Among them, GPXs play an important role in regulating the intracellular redox homeostasis by scavenging H_2O_2 and soluble phospholipid hydroperoxide using glutathione (GSH) as a reducing substrate, thereby preserving the cellular structural integrity and function [12]. GPX1, an important isoform in the GPX family, is located in the cytosol and mitochondria and protects the mitochondria from ROS [13]. GPX1 overexpression considerably attenuated the total intracellular and mitochondrial ROS levels and effectively improved the remodeling of the glomerular and tubule proteomes in the kidneys of old mice by preserving antioxidant activities [14]. Moreover, the knockdown of GPX1 in ATDC5 cells not only inhibited their proliferation but also impaired chondrogenic differentiation by increasing oxidative and reductive stress, thus possibly promoting the pathogenesis of endemic osteoarthritis [15]. Considering that IVDD shares several pathophysiological characteristics with osteoarthritis, GPX1 represents a potential therapeutic target for preventing IVDD.

Notably, GPX1 is a selenoprotein that contains the amino acid selenocysteine at its active site, which represents the main form of selenium in the human body. Selenium is an essential trace element that is vital for redox homeostasis via its incorporation into various antioxidant enzymes that scavenge free radicals and antagonize heavy metals [16]. A recent study from our laboratory suggested that the supplementation with sodium selenite, which is an inorganic form of selenium, promoted the repair of osteoporotic bone defects by activating the GPX1-mediated mitochondrial antioxidant pathway

[17]. However, high-dose sodium selenite can cause serious toxicity issues, thus limiting its therapeutic application [18]. Alternatively, selenium nanoparticles (SeNPs) have been attracting immense attention because of their unique physical properties, including their nano size and surface effect, and their remarkable antioxidant and anti-inflammatory activities, without the induction of side effects [19]. Compared with other Se compounds such as selenite and selenomethionine, SeNPs exhibit favorable biocompatability while enhancing selenoenzyme activities [20]. Ouyang et al. reported that SeNPs encapsuled in hyaluronic acid hydrogel microbeads can synthesize selenoproteins in situ and effectively alleviate colitis-associated symptoms by reducing the secretion of pro-inflammatory cytokines [21]. However, the therapeutic effect of SeNPs on IVDD and the mechanisms involved in the GPX1 antioxidant pathway remain unknown.

Herein, we hypothesize that SeNPs can ameliorate IVDD by maintaining the matrix metabolism and improving the mitochondrial antioxidant functions of NPCs. SeNPs were synthesized by reducing sodium selenite in gelatin, which acts as a natural stabilizer and size-controlling agent, followed by dialysis to purify the nanoparticles. The morphology, size distribution, elemental analysis, biocompatibility, and cellular uptake efficiency of the prepared SeNPs were characterized. The protective effects of SeNPs on matrix synthesis and degradation, mitochondrial energy metabolism, and intracellular antioxidant ability, particularly in the presence of interleukin 1 beta (IL-1β), were investigated. RNA sequencing and the small interfering RNA (siRNA) technique were used to elucidate the antioxidant mechanism involving the GPX1 selenoprotein. Furthermore, the therapeutic efficacy of SeNPs on puncture-induced NP degeneration in a rat lumbar IVD model was evaluated. This study reports a strategy that utilizes SeNPs with favorable antioxidant properties for the enhancement of mitochondrial function and treatment of IVDD (Scheme 1).

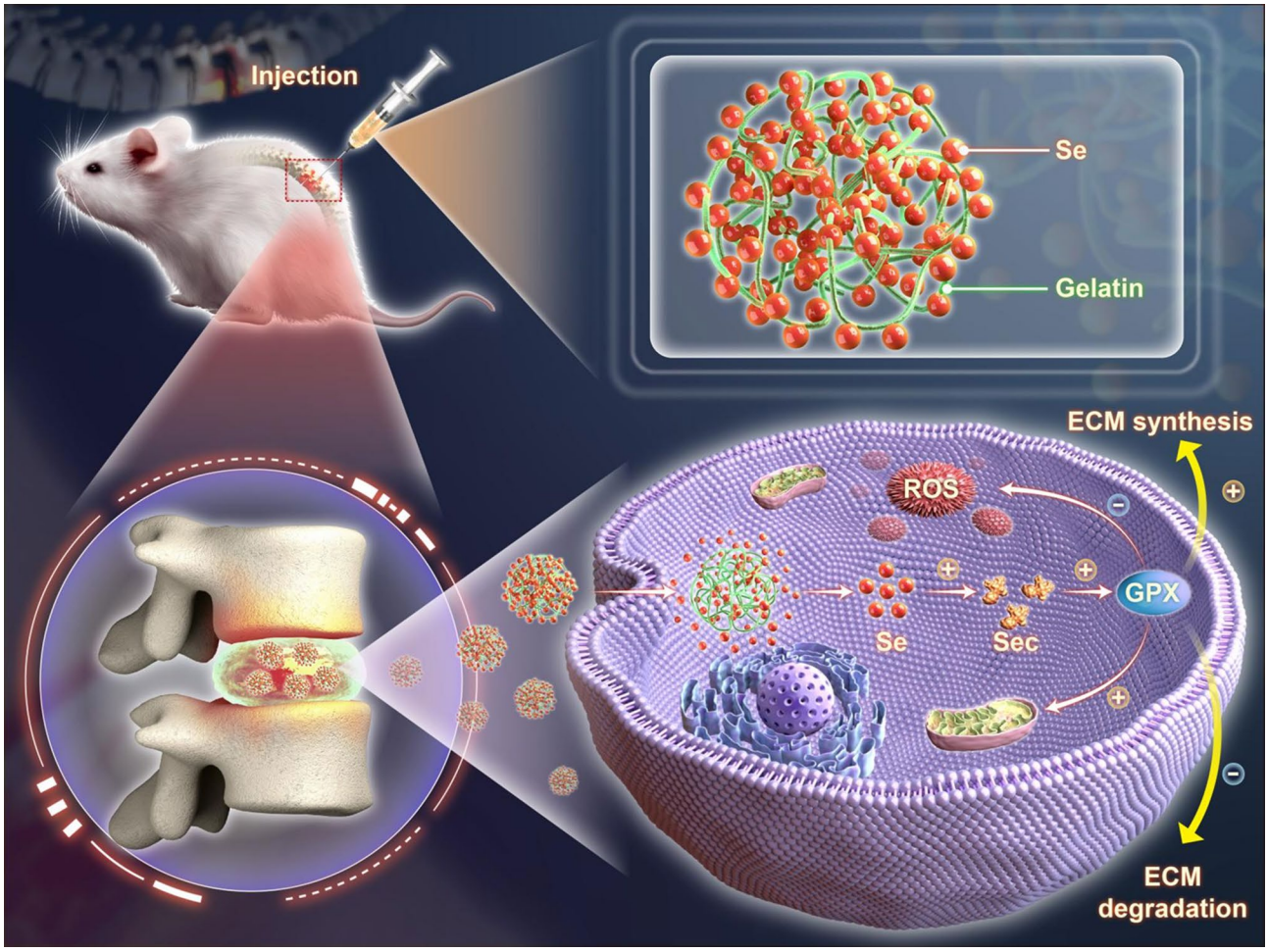

Scheme 1 Schematic illustration of SeNPs ameliorating rat lumbar disc degeneration. SeNPs enhance expression of GPX1 and mitochondrial function of NPCs. After injection administration, SeNPs significantly promote GPX1 expression, thereby improving mitochondrial function and decreasing ROS level. SeNPs ameliorate lumbar disc degeneration by increasing matrix synthesis and inhibiting matrix degradation

Results

Characterization of SeNPs

In this study, SeNPs were prepared using a simple chemical synthesis method. Transmission electron microscopy (TEM) images revealed that the prepared SeNPs were uniformly dispersed and spherical, with an average size of approximately 60 nm (Fig. 1A). Element mapping further shows that the Se and S elements are distributed in the framework of selenium nanoparticles, with high uniformity (Fig. 1B). X-ray photoelectron spectroscopy (XPS) verified the presence of carbon (C), nitrogen (N), oxygen (O), and selenium (Se), without significant impurities (Fig. 1C, D). The Se 3d5/2 and 3d3/2 peaks are observed at 55.32 and 56.12 eV in peak fitting analysis, respectively. This result confirmed that the oxidation state of Se in our material is Se^0 and there were no other oxidation states, which proved the monatomic morphology of Se in the material (Fig. 1E). The mean hydrodynamic particle size of SeNPs is 166.4 nm, and the size distribution is narrow (particle dispersion index [PDI]: 0.205), indicating that these particles have good dispersion in the water medium (Fig. 1F). Fourier transform-infrared spectrometry (FT-IR) has a distinct characteristic peak at 3267 cm^{-1} (Fig. 1G), which is attributed to the amidogen (N-H) in the gelatin. The characteristic peak at 1634 cm^{-1} indicates the presence of carbonyl groups (C=O) in the mix of gelatin and SeNPs. However, by comparing the gelatin without Se, the FT-IR result were basically the same, which indicated the two chemical groups came from the gelatin instead of SeNPs (Additional file 1: Figure S1A). By labeling SeNPs with cy5, we observed that their fluorescence intensity dependent on the concentration after the ingestion of selenium nanoparticles by the NPC (Fig. 1H). The uptake rate of control group is 0 and the uptake rate was higher at a concentration of 50 ng/mL (Additional file 1: Figure S1B). Taken together, these results confirm the successful simple synthesis method for production of SeNPs.

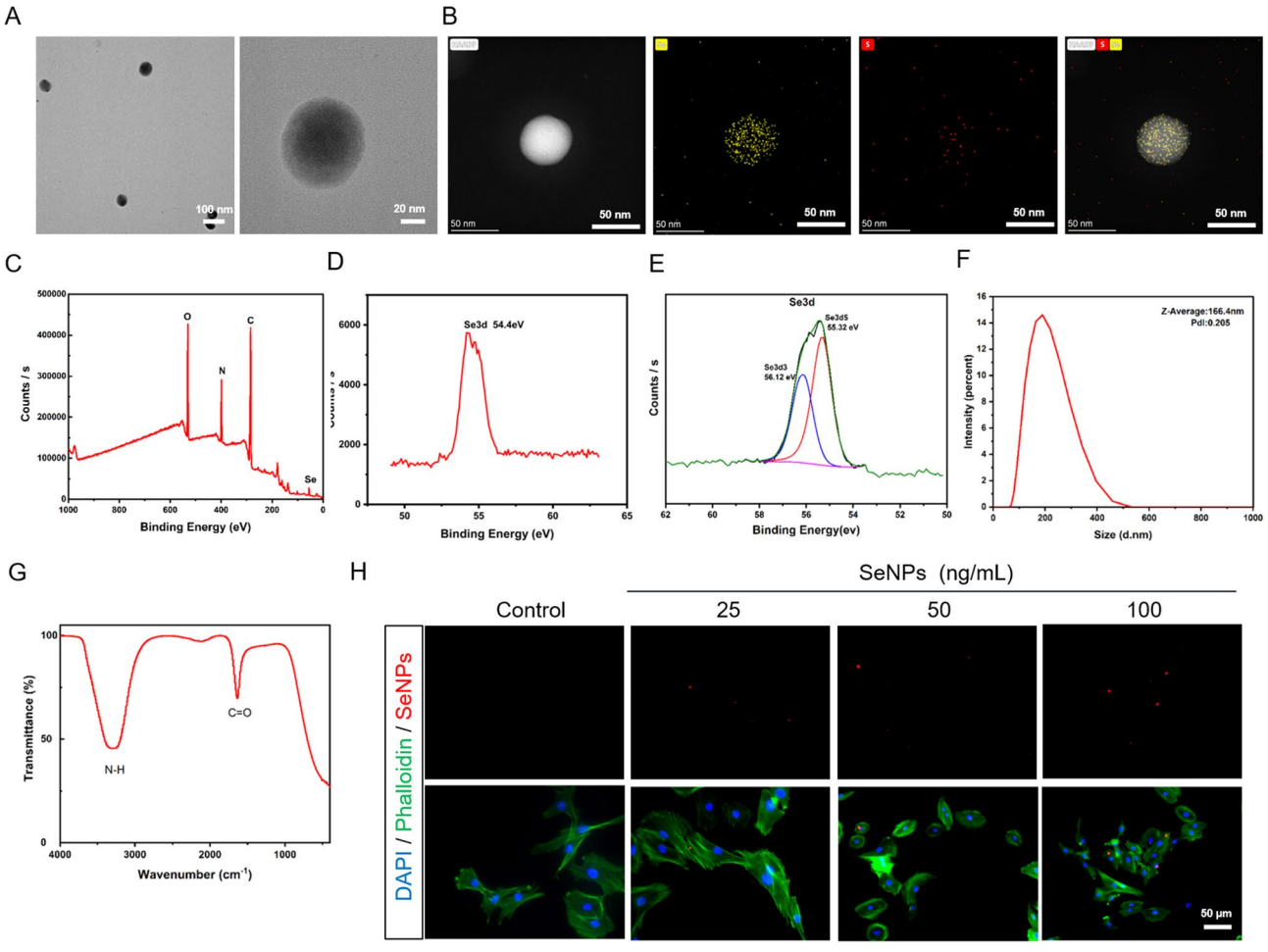

Fig. 1 Characteristics of SeNPs. **A** TEM images showed the intuitional characteristic of SeNPs. **B** The element mapping of Se and S elements in SeNPs. **C**, **D** XPS confirmed the presence of C, N, O, and Se in SeNPs. E Peak fitting analysis of Se in XPS. **F** The average hydrodynamic particle diameter of SeNPs. **G** FT-IR showed two characteristic peaks at 3267 cm^{-1} and 1634 cm^{-1}, respectively. **H** SeNPs (labeled with cy5) entering NPCs at different concentrations were observed

Effects of SeNPs on cell proliferation and matrix metabolism of NPCs

The biocompatibility of SeNPs was further evaluated. The live/dead staining showed that, after incubation with 25, 50, and 100 ng/mL SeNPs for 5 days, the cell viability of NPCs was higher than 98.5% (alive cells indicated by green fluorescence) with negligible cytotoxicity (dead cells indicated by red fluorescence) (Fig. 2A, B). Cell Counting Kit-8 (CCK-8) assays confirmed that, compared with the control group, 25 and 50 ng/mL SeNPs significantly increased the cell proliferation of NPCs on day 5 by 7.6% and 11.7%, respectively (Fig. 2C). To evaluate the influence of SeNPs on the matrix metabolism of NPCs, we investigated the levels of three ECM synthesis genes (*Acan*, *Col2a1*, and *Sox9*) and two ECM degrading genes (*Mmp13* and *Adamts5*). SeNPs significantly increased the expression of ECM synthesis genes at the concentrations of 25 and 50 ng/mL, wheres 100 ng/mL SeNPs reduced their transcriptive levels. Notably, the 50 ng/mL group yielded the highest levels of ECM synthesis genes, in which the mRNA levels of *Acan* (aggrecan) was upregulated by 40.2%, *Col2a1* (type II collagen) by 79.4%, and *Sox9* by 32.5%, respectively, compared with the control group (Fig. 2D). Western blot analysis confirmed that 50 ng/mL SeNPs strongly promoted the protein expression of ACAN by 17.4%, COL2A1 by 41.7%, and SOX9 by 20.1%, respectively, compared with the control group (Fig. 2E, Additional file 1: Figure S2A). Considering the important role of ACAN in maintaining nucleus pulposus hydration, immunofluorescence staining for ACAN

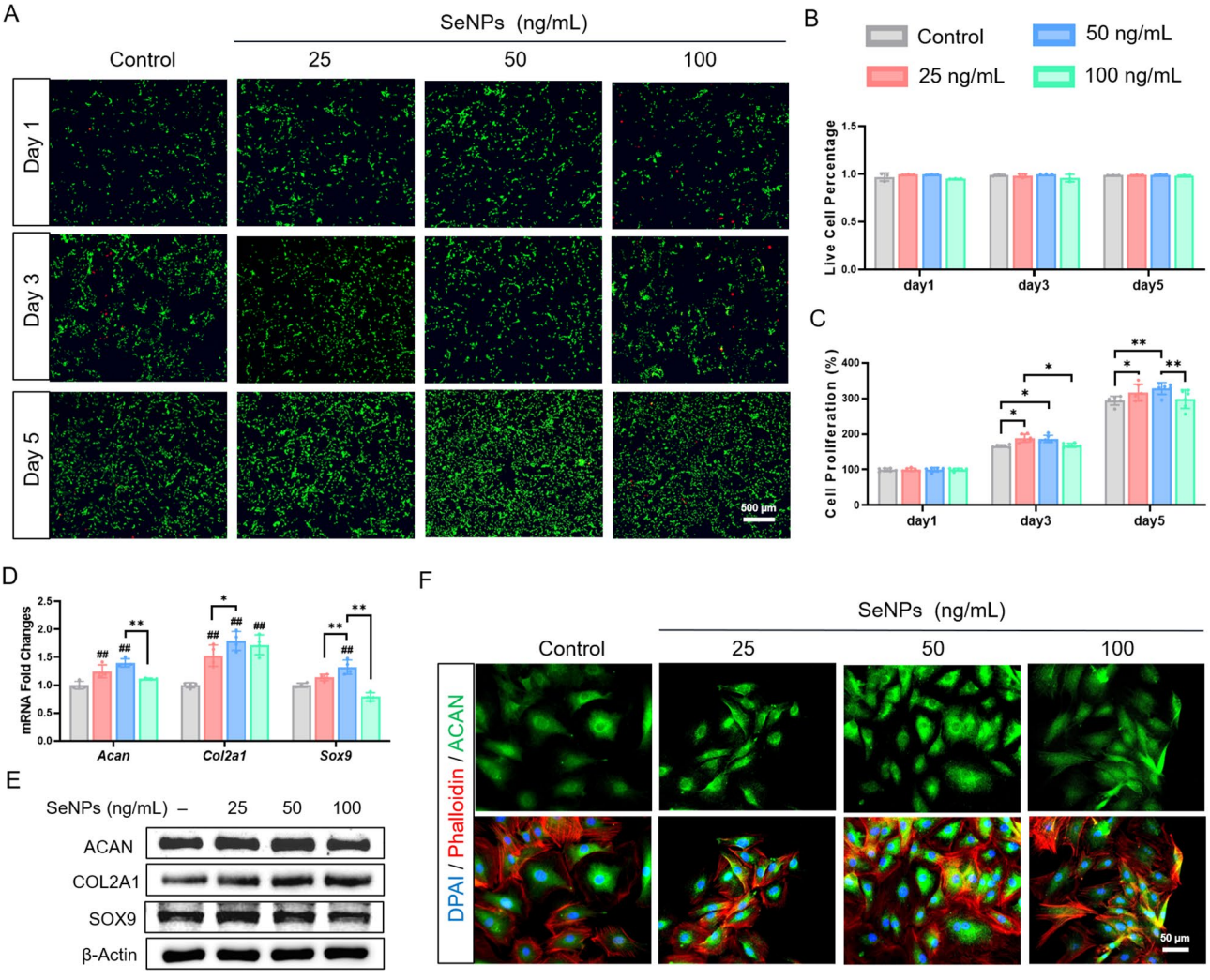

Fig. 2 Effect of SeNPs on cell proliferation and matrix synthesis of normal NPCs. NPCs were treated with SeNPs concentrations of 25,50 and 100 ng/mL. **A** The activity of the NPCs at day 1, 3, and 5 was evaluated using live/dead staining. **B** Quantitative results of live/dead staining. ($n=3$) **C** The proliferation of cells was detected by CCK-8 assays. ($n=6$) **D** Quantitative RT-PCR was used to determine the mRNA levels of nucleus pulposus matrix genes *Acan*, *Col2a1* and *Sox9*. ($n=4$) **E** Western blotting was used to determine the effects of the SeNPs on the levels of aggrecan, type II collagen and SOX9 protein in NPCs. **F** Immunofluorescence staining of aggrecan showed the matrix synthesis ability of NPCs. Statistically significant differences are indicated by # where $P<0.05$ or ## where $P<0.01$ compared with the control group; * where $P<0.05$ or ** where $P<0.01$ between the indicated group

was performed that was consistent with its mRNA levels (Fig. 2F, Additional file 1: Figure S2B). In addition, no significant difference in cytoskeletal size between the four groups (Additional file 1: Figure S2B). In terms of matrix degradation, the mRNA levels of *Mmp13* (matrix metalloproteinase 13) were down-regulated by 43.1% at 25 ng/mL, 68.2% at 50 ng/mL, and 69.1% at 100 ng/mL, respectively, compared with the control group (Additional file 1: Figure S2C). The protein levels of MMP13 and ADAMTS5 (a disintegrin and metalloproteinase with thrombospondin motifs 5) showed a consistent decrease along with their mRNA expression (Additional file 1: Figure S2D, E).

SeNPs improved mitochondrial function of NPCs

TEM was utilized to observe the changes in mitochondrial morphology in SeNP-treated NPCs. Compared with the control group, treatment with 50 ng/mL SeNPs resulted in an increase in the cristae number and structure, indicating that SeNP intervention probably improved the activity of mitochondrial energy metabolism (Fig. 3A). Consistently, the intracellular ATP content in SeNP-treated NPCs (50 ng/mL) was 14.7% higher than that of the control group (Fig. 3B). We continued to investigated the membrane potential changes, as an increase in mitochondrial permeability leads to concomitant mitochondrial dysfunction and apotosis. JC-1 staining demonstrated that SeNP treatments dose-dependently increased the red-green fluorescence ratio of NPCs by 60.6% at 25 ng/mL, 121.6% at 50 ng/mL, and 92.1% at 100 ng/mL, respectively (Fig. 3C, Additional file 1: Figure S3A). Mitochondria play a vital role in the cellular energy metabolism and a series of oxidative respiratory chain genes, including *Sdha* (succinate dehydrogenase complex flavoprotein subunit A), *Atp5* (ATP synthase subunit 5), *Nd4* (NADH dehydrogenase subunit 4), and *Cox4* (cytochrome c oxidase subunit IV), were up-regulated by the SeNP treatments. Notably, 50 ng/mL SeNPs significantly increased the mRNA levels of *Sdha* by 5.4-fold, *Atp5* by 4.7-fold, *Nd4* by 5.2-fold, and *Cox4* by 3.0-fold, respectively, compared with the control group (Fig. 3D). Western blot confirmed the protein levels of these four respiratory chain factors were up-regulated by SeNPs (Fig. 3E, Additional file 1: Figure S3B). These results suggested that treatment with SeNP, particularly at 50 ng/mL, preserved the integrity of mitochondria and improved the mitochondrial energy metabolism in NPCs. Therefore, we selected 50 ng/mL for subsequent experiments.

SeNPs maintained ECM metabolism and mitochondrial homeostasis of NPCs in the Presence of IL-1β

The inflammatory environment induced by IL-1β remarkably suppressed the expression of ACAN, whereas treatment with SeNPs (50 ng/mL) strongly protected its expression, as indicated by the immunofluorescence staining (Fig. 4A, Additional file 1: Figure S4A). There was no significant difference in cytoskeleton size between the three groups (Additional file 1: Figure S4A). Consistently, the protective effect of SeNPs on the synthesis of ECM components (e.g. ACAN and COL2A1) was confirmed at both the mRNA (Additional file 1: Figure S4B) and protein levels (Additional file 1: Figure S4C, D). Importantly, the expression of two matrix catabolic enzymes MMP13 and ADAMTS5 was dramatically increased by IL-1β, but SeNP treatment effectively reduced their levels. For example, SeNPs significantly down-regulated MMP13 by 39.6% at the transcriptive level (Fig. 4B) and 47.8% at the protein level compared to the IL-1β group (Fig. 4C, Additional file 1: Figure S4E). These results suggested that treatment with SeNPs can restore the balance between matrix anabolism and catabolism in NPCs that was disturbed by the inflammatory cytokine IL-1β.

We further investigated the protective effect of SeNPs on mitochondrial morphology and function. As shown in Fig. 4D, mitochondria in IL-1β-treated NPCs exhibited a swollen shape with decreased number of cristae and even rupture of outer mitochondrial membrane. Treatment with SeNPs successfully retrieved the rod-shaped morphology with prominent mitochondrial cristae and clearly visible mitochondiral ridges. In the IL-1β group, NPCs displayed a 12.1% reduction in the ATP production compared to the control group, implying a significant impact of inflammatory environment on energy metabolism. However, SeNP treatment improved the ATP production by 6.9% compared to the IL-1β group (Fig. 4E). Images of JC-1 staining showed a low red/green fluorescence ratio in the IL-1β group, indicative of $\Delta\Psi m$ depolarization. In contrast, treatment with SeNPs significantly increased the $\Delta\Psi m$ as indicated by a relatively high red/green fluorescence ratio, reflecting an improvement of mitochondrial permeability (Fig. 4F, Additional file 1: Figure S4F). We examined the impact of IL-1β and SeNPs on the expression of mitochondrial respiratory chain factors. Compared to the control group, exposure of NPCs to IL-1β resulted in a significant reduction in both the mRNA and protein levels of SDHA, ATP5, ND4, and COX4. However, the administration of SeNPs effectively preserved the expression of these four factors (Fig. 4G, H, Additional file 1: Figure S4G). These results proved the protective effects of SeNPs on mitochondrial membrane integerity and energy metabolism of NPCs in the inflammatory environment.

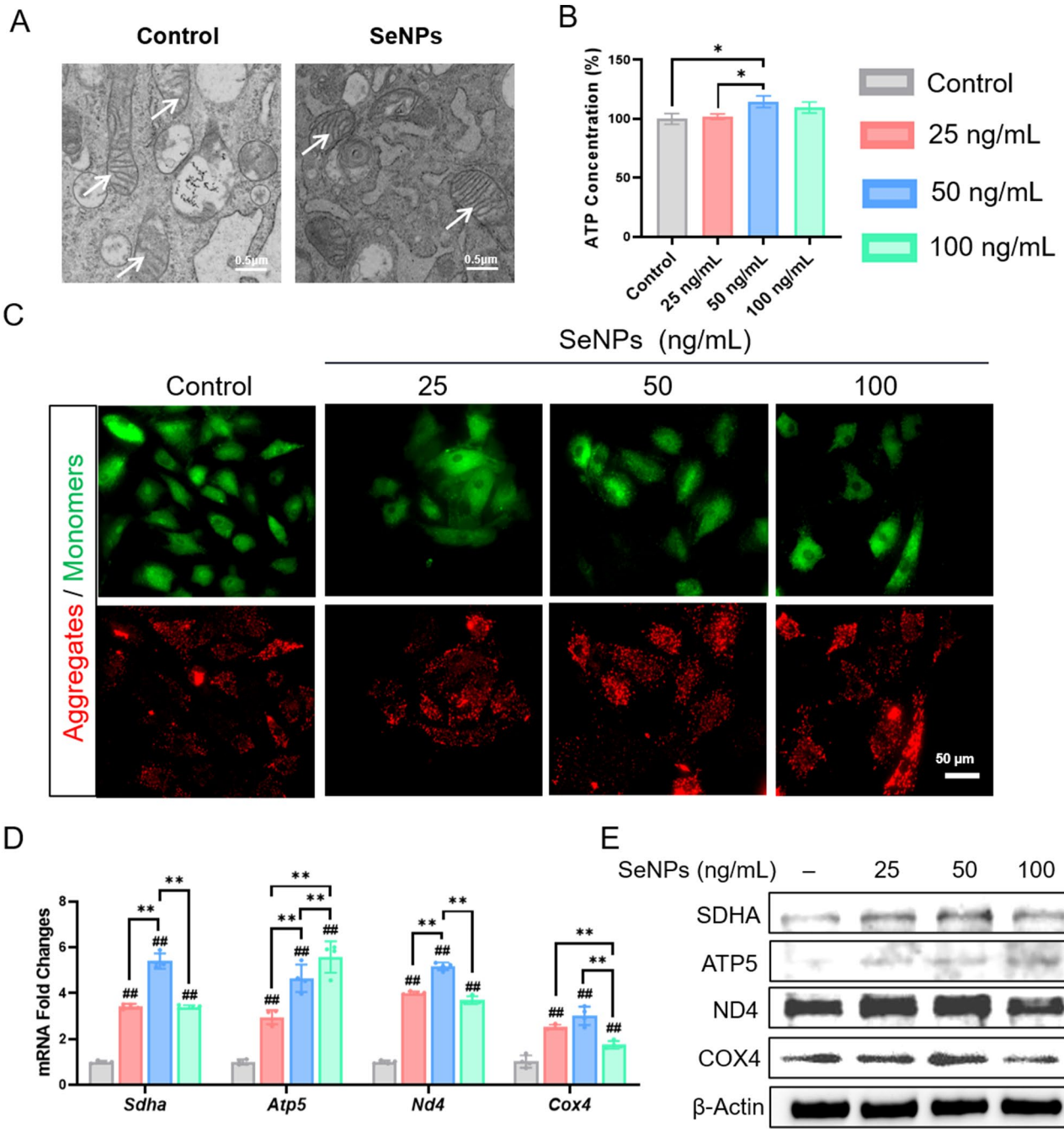

Fig. 3 Effect of SeNPs on mitochondrial function of normal NPCs. NPCs were treated with SeNPs concentrations of 25,50 and 100 ng/mL. **A** Transmission electron microscopy images of intracellular mitochondria of NPCs. **B** Effect of SeNPs on ATP content in NPCs. **C** JC-1 fluorescence staining results of NPCs under different concentrations of intervention of SeNPs. **D** Quantitative RT-PCR was used to determine the mRNA levels of genes *Sdha*, *Atp5*, *Nd4* and *Cox4*. ($n=4$) **E** Western blotting was used to determine the effects of the SeNPs on the levels of protein SDHA, ATP5, ND4 and COX4 in NPCs. Statistically significant differences are indicated by # where $P<0.05$ or ## where $P<0.01$ compared with the control group; * where $P<0.05$ or ** where $P<0.01$ between the indicated group

RNA sequencing analysis of NPCs after SeNP treatment

RNA sequencing of NPCs treated with SeNPs was performed. Overall, heat maps showed that a total of 75 differentially expressed genes, including 60 upregulated and 15 downregulated genes, were identified in NPCs treated with SeNPs compared with the controls (Fig. 5A). Encouragingly, We found that the *Gpx1* gene was significantly activated. Gene ontology (GO) pathway enrichment analysis revealed that several pathways, such as

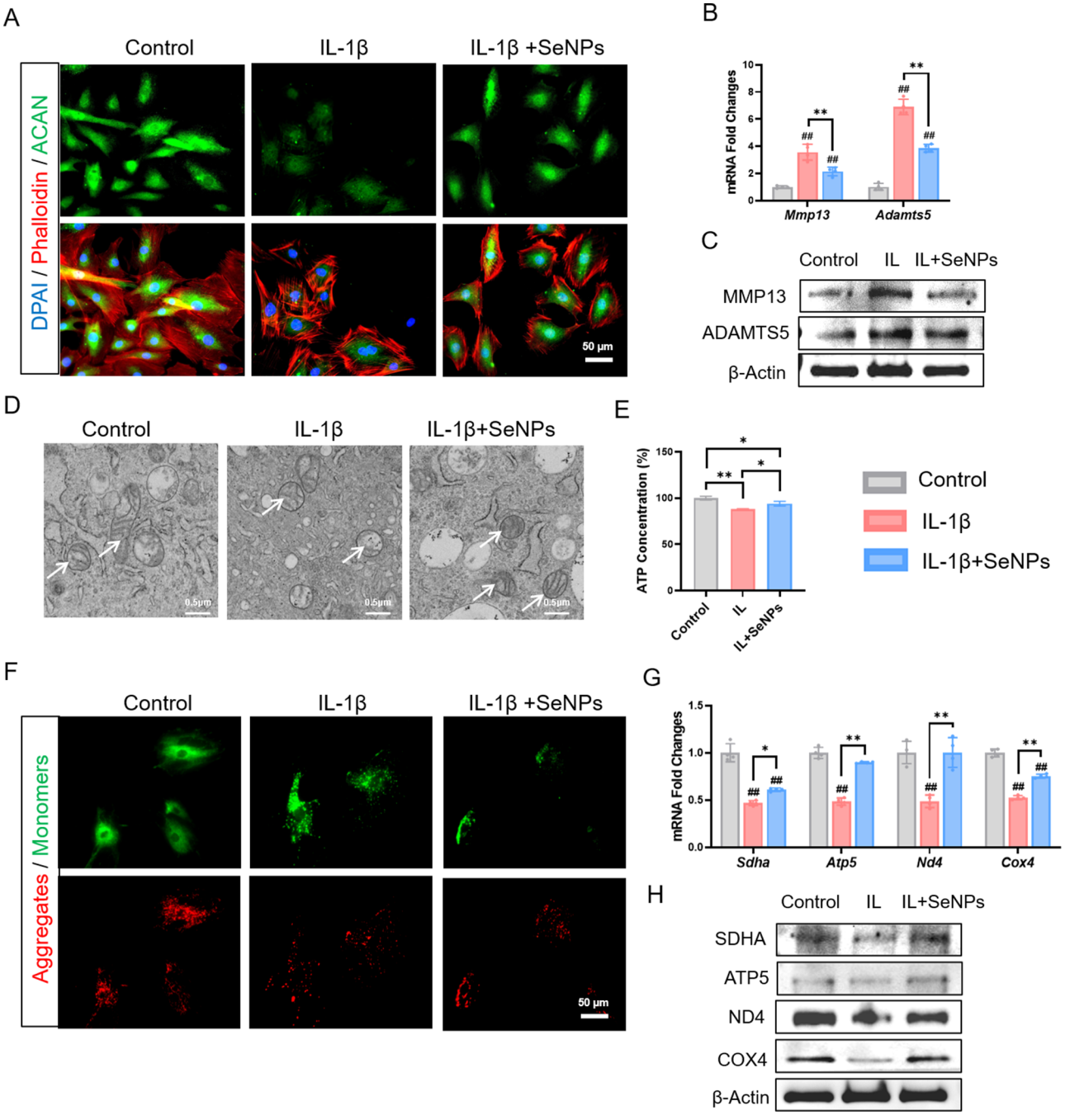

Fig. 4 SeNPs have a protective effect on NPCs in the inflammatory environment caused by IL-1β. **A** Immunofluorescence staining of aggrecan in NPCs. **B** Quantitative RT-PCR was used to determine the mRNA levels of nucleus pulposus matrix genes *Mmp13* and *Adamts5*. ($n=4$). **C** Western blotting was used to determine the levels of MMP13 and ADAMTS5 protein in NPCs. **D** Transmission electron microscopy images of intracellular mitochondria of NPCs. **E** Effect of SeNPs on ATP content in NPCs under inflammatory environment. **F** JC-1 fluorescence staining results of NPCs under inflammatory environment. **G** Quantitative RT-PCR was used to determine the mRNA levels of genes *Sdha*, *Atp5*, *Nd4* and *Cox4*. ($n=4$) **H** Western blotting was used to determine the effects of the SeNPs on the levels of protein SDHA, ATP5, ND4 and COX4 in NPCs under inflammatory environment. Statistically significant differences are indicated by # where $P<0.05$ or ## where $P<0.01$ compared with the control group; * where $P<0.05$ or ** where $P<0.01$ between the indicated group

matrix-synthesis signaling pathway, the glutathione metabolic process, and mitochondrion were closely associated with the therapeutic mechanism of SeNPs (Fig. 5B). Moreover, the Kyoto Encyclopedia of Genes and Genomes (KEGG) enrichment analysis demonstrated that pathways related to glycosaminoglycan biosynthesis were significantly enriched in the SeNPs group (Fig. 5C). GSEA indicated that SeNPs treatment can upregulate the

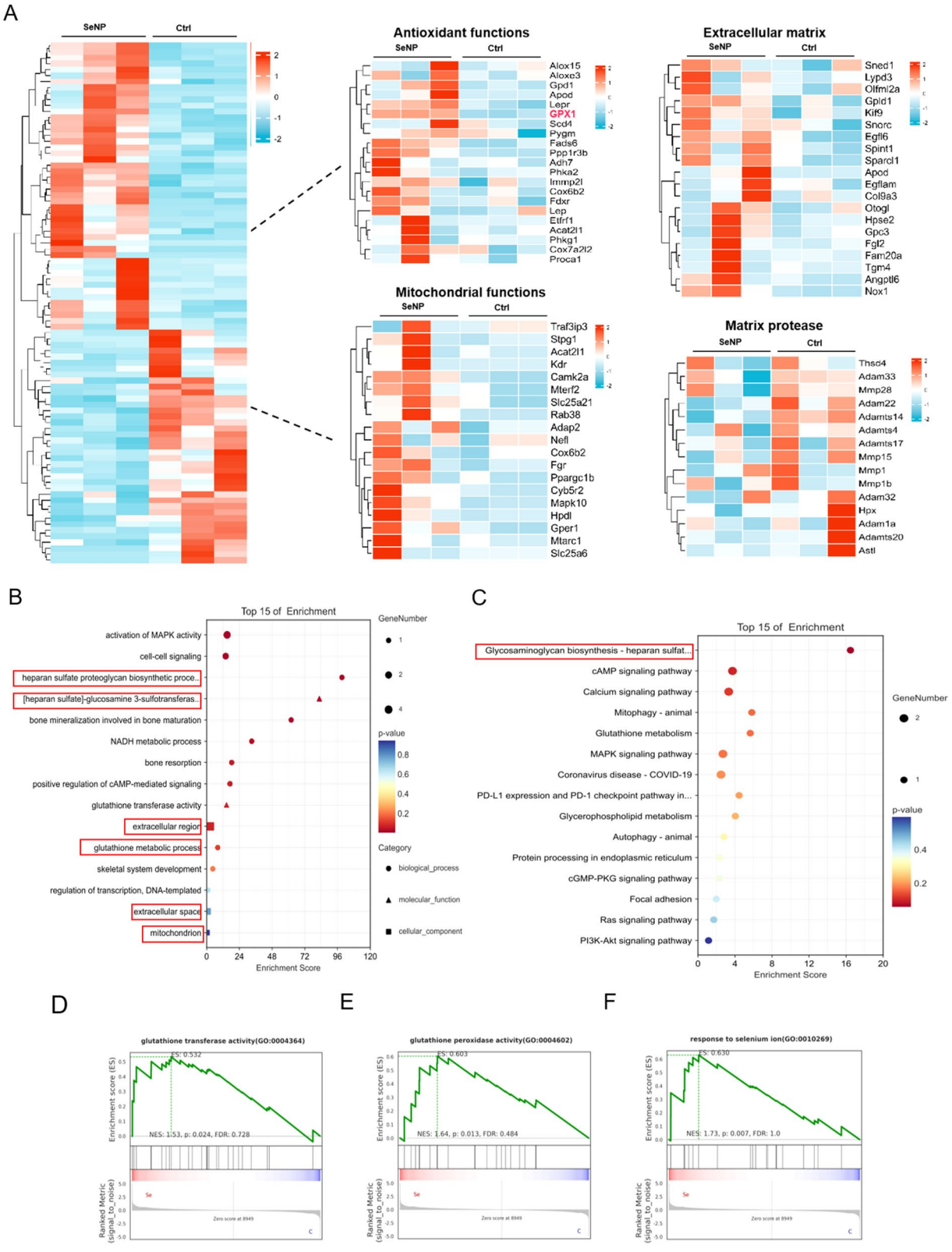

Fig. 5 RNA sequencing analysis of NPCs with SeNPs intervention. **A** Heatmap of differentially expressed gene between control group and SeNPs intervention group. **B** GO enrichment analysis of biological processes and cellular component illustrated the count of the up- and down-regulated genes (indicated by the lines). **C** KEGG analysis revealed the up and down-regulated signaling pathways in NPCs. **D**, **E**, **F** GSEA enrichment analysis of glutathione transferase activity ($p = 0.0024$), glutathione peroxidase activity ($p = 0.013$), and response to selenium ion ($p = 0.007$) between the control and SeNPs groups

activities of GPX and glutathione transferase, as was the response to selenium particles (Fig, 5D-F). SeNPs treatment can upregulate GPX and glutathione transferase, suggesting its potential to reduce ROS-induced cell damage and restore mitochondrial function. In summary, SeNPs interfered with NPCs, which significantly promoted GPX expression and enhanced the matrix-synthesis ability and mitochondrial metabolic function.

SeNPs alleviated IL-1β-induced oxidative stress via activating antioxidant selenoproteins

Since redox homeostasis is closely associated with mitochondrial function, we studied the scavenging ability of SeNPs on intracellular and mitochondrial ROS in IL-1β-exposed NPCs using immunofluorescence staining (Fig. 6A). Compared to the IL-1β group, the levels of intracellular (indicated by DCFDA fluorescence) and mitochondrial ROS (indicated by MitoSOX fluorescence) in SeNP-treated NPCs were significantly attenuated by 23.3% and 19.7%, respectively (Fig. 6A, B, Additional file 1: Figure S5A, B). To unravel the underlying mechanism involved antioxidant enzymes, we further examined the expression of three important selenoproteins, GPX1, TXNRD1 (thioredoxin reductase 1), and TXNRD2 (thioredoxin reductase 2). Treatment with SeNPs significantly up-regulated the transcriptive levels of *Gpx1* by 4.2-fold, *Txnrd1* by 1.7-fold, and *Txnrd2* by 2.8-fold, respectively, compared to those of the IL-1β-exposed NPCs (Fig. 6C). Similarly, Western blot analysis confirmed the beneficial effect of SeNPs on the three selenoproteins (Fig. 6D, Additional file 1: Figure S5C). Considering the role of GPX1 in mitochondrial antioxidant functions,

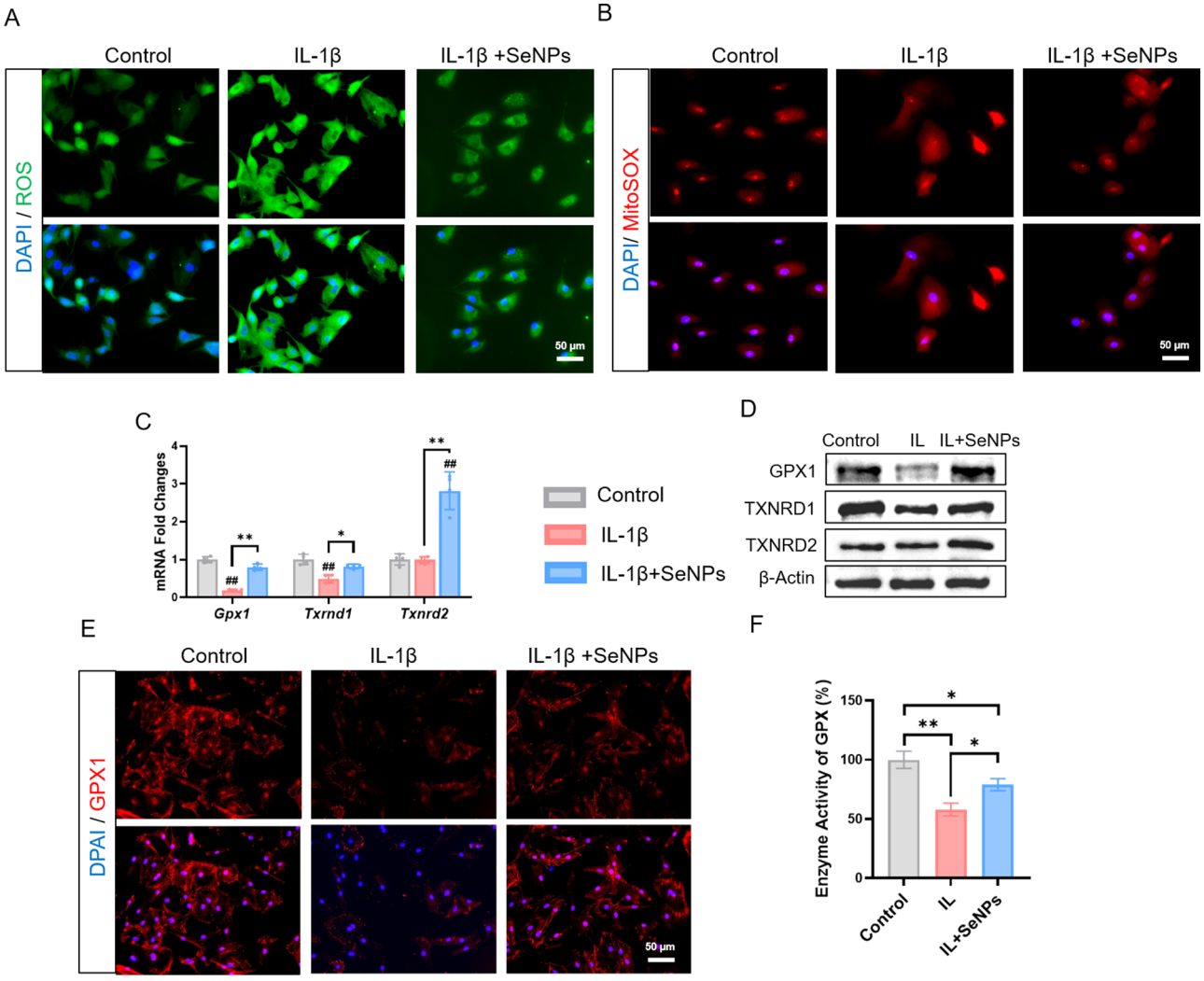

Fig. 6 **A** Intracellular ROS levels in NPCs. **B** MitoSOX levels in mitochondria of NPCs. **C** Quantitative RT-PCR was used to determine the mRNA levels of genes *Gpx1*, *Txnrd1* and *Txnrd2*. ($n = 4$) **D** Western blotting was used to determine the levels of GPX1, TXNRD1 and TXNRD2 protein in NPCs. **E** Immunofluorescence staining of GPX1 of NPCs in inflammatory environment. **F** GPX-like activity of NPCs. Statistically significant differences are indicated by # where $P < 0.05$ or ## where $P < 0.01$ compared with the control group; * where $P < 0.05$ or ** where $P < 0.01$ between the indicated group

immunofluorescence staining was performed and SeNPs treatment effectively restored the expression and distribution of GPX1 in IL-1β-exposed NPCs (Fig. 6E, Additional file 1: Figure S5D). Consistently, in the IL-1β group, the activity of GPX1 was decreased by 42.0% but it was increased by 36.3% after treating with SeNPs (Fig. 6F). These results suggested that SeNPs attenuated IL-1β-induced oxidative stress through activation of antioxidant selenoproteins, in particular GPX1.

Silencing of GPX1 reversed the protective effect of SeNPs on NPCs

To gain further insights into the role of GPX1 in SeNP-mediated protection, NPCs were first transfected with si-RNA targeting *Gpx1*, we set up three groups: negative control (NC) group, si-*Gpx1* group and si-*Gpx1*+SeNPs (50 ng/mL) group. The transfection of si-*Gpx1* significantly down-regulated the mRNA expression of *Gpx1* by 47.26% compared to the NC group, but there was no significant difference between si-*Gpx1* group and si-*Gpx1*+SeNPs group (Fig. 7A). Consistently, the protein expression of GPX1 was decreased by 53.7% and 50.3% (Fig. 7B, Additional file 1: Figure S6A), respectively, in si-*Gpx1* group and si-*Gpx1*+SeNPs group. The transfection of si-*Gpx1* abrogated the protective effects of SeNPs on mitochondrial energy metabolism, as evidenced by the down-regulation of four respiratory chain factors, SDHA, ATP5, ND4, and COX4, at both mRNA (Fig. 7C) and protein levels (Fig. 7D, Additional file 1: Figure S6B). Furthermore, silencing of *Gpx1* inhibited the synthesis of ACAN in NPCs, even treated with SeNPs. Compared with the NC group, the transfection of si-*Gpx1* significantly reduced the transcriptive levels of *Acan* by 19.2% and *Col2a1* by 31.4%, respectively, in SeNP-treated cells (Fig. 7E). Western blotting confirmed the down-regulation of these ECM synthesis proteins (Fig. 7F, Additional file 1: Figure S6A). Therefore, silencing of *Gpx1* abolished SeNP-mediated protection on the matrix synthesis capacity and mitochondrial respiratory function of NPCs, indicating the crucial role of GPX1 in regulating matrix and energy metabolism.

In Situ administration of SeNPs preserved the hydration of nucleus pulposus and ameliorated rat lumbar disc degeneration

To assess the therapeutic efficacy of SeNPs in treating IVDD, a needle puncture model was established on rats' lumbar discs (Additional file 1: Figure S7A), and two different dosages of SeNPs (25 and 50 ng/mL) were injected in situ into the injured discs (Fig. 8A). At 8 weeks postsurgery, histological analysis demonstrated that there was no pathological changes in the heart, liver, spleen, lung, and kidney in the SeNP-50 ng/mL compared with the control group, suggesting that 50 ng/mL SeNPs was a safe dosage for IVD in situ injection (Figure S7B, Supporting Information).

At 4 and 8 weeks postsurgery, imaging techniques and histological analysis were employed to evaluate the hydration and matrix degradation in each group. Magnetic resonance imaging (MRI), as the gold standard for IVDD diagnosis, was used to evaluate the water content in the nucleus pulposus. In the Sham group, hyperintensity on T2-weighted images were observed that was associated with a high level of water content. After the needle puncture, the MRI signals of the lumbar discs reduced in the IVDD group, indicating that the degeneration lead to a loss of water content and remodeling of IVD matrix. Conversely, both the SeNP-25 and SeNP-50 groups showed greater signal intensity (Fig. 8B). Pfirrmann grading scores confirmed that the improvement of IVD hydration in the SeNP-25 and SeNP-50 groups at 8 weeks postsurgery that were 19.2% and 42.3% higher than that in the IVDD group (Fig. 8D). With regard to disc height, qualitative analysis of X-ray images revealed a significant reduction of 22.9% in disc height index (DHI) in the IVDD group compared to the Sham group. However, treatment with SeNPs effectively rescued the height of punctured discs (Fig. 8C). In particular, the SeNP-50 group exhibited the lowest decrease in DHI at 8 weeks post-surgery (31.9% higher than that of the IVDD group) that resembled the Sham group (Fig. 8E). These imaging results suggested that administration of SeNPs had the potential to delay IVDD by preserving the disc height and hydration of IVDs.

Histology evaluation of the therapeutic efficacy of SeNPs on punctured-induced IVDD

Histological analysis, including H&E and S.O. staining, was performed to observe the structure and matrix deposition of the degenerated IVDs treated with SeNPs. H&E staining revealed a significant decrease in the cell number of NPCs and collapsed NP tissues in the IVDD group. The administration of SeNPs, in particular at the dosage of 50 ng/mL, largely maintained the structure integrity of the punctured IVDs at postoperative 4 and 8 weeks, as evidenced by the clear boundary between the nucleus pulposus and annulus fibrosus (Fig. 9A). S.O. staining showed that, compared to the Sham group, the composition of GAGs in the NP tissue was markedly reduced that was replaced with fibrous tissue in the IVDD group. The treatment with SeNPs effectively perserved the GAG content in the NP tissue that was similar to the Sham group (Fig. 9A). Masson's Trichrome showed that the change of collagen deposition in the IVDD and Sham groups at postoperative 4 and 8 weeks was consistent to the results of S.O. staining (Fig. 9A). The histological scores, as shown in Fig. 9B, were significantly increased in the IVDD group, but were 15.9% and 29.5% lower in

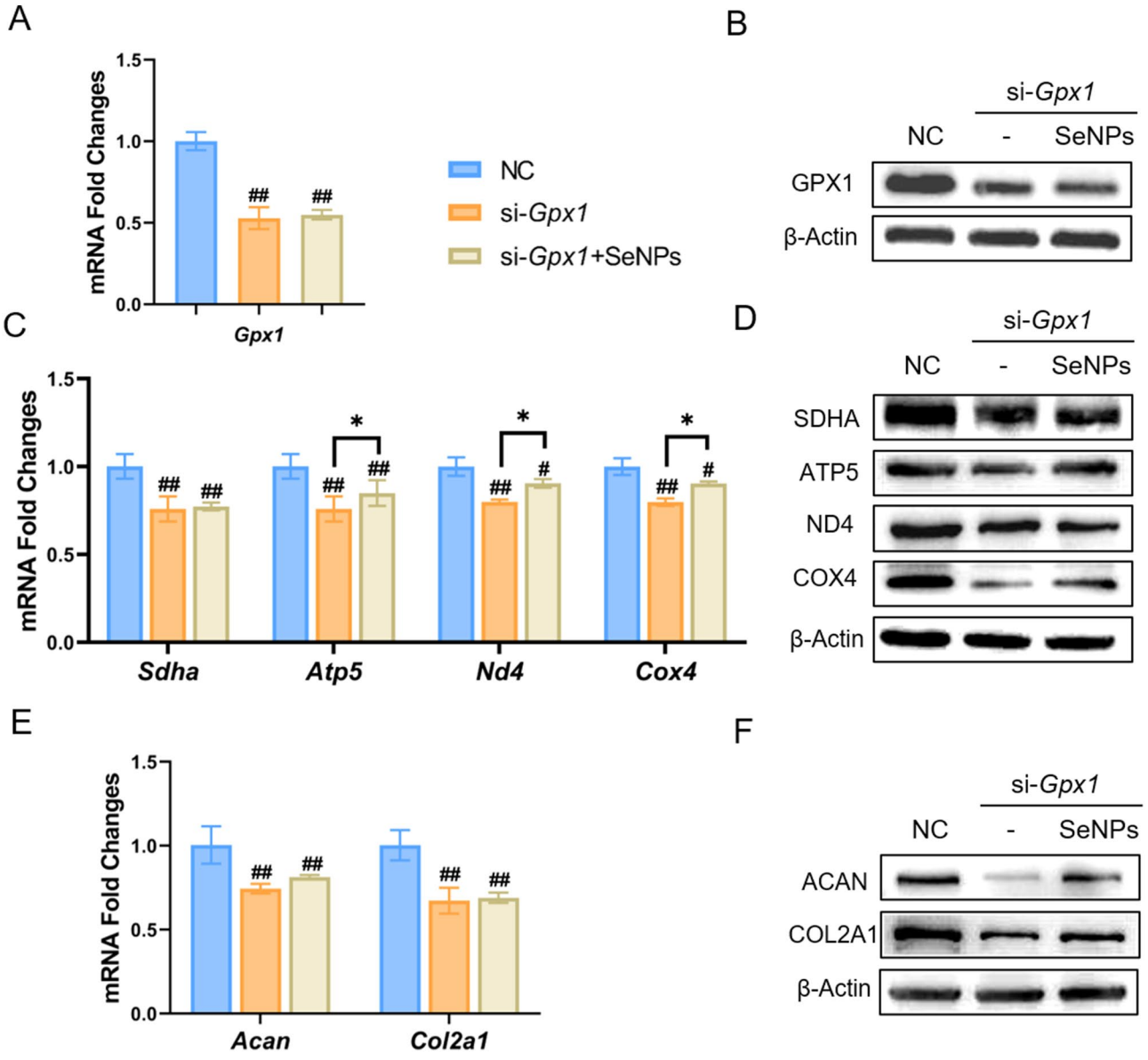

Fig. 7 Effect of SeNPs on NPCs under GPX1 gene silencing experiment. **A** Quantitative RT-PCR was used to determine the mRNA levels of *Gpx1* gene. ($n=4$) **B** Western blotting was used to determine the levels of GPX1 protein in NPCs. **C** Quantitative RT-PCR was used to determine the mRNA levels of genes *Sdha*, *Atp5*, *Nd4*, and *Cox4* in NC, si-*Gpx1* and si-*Gpx1* + SeNPs groups. ($n=4$) **D** Western blotting was used to determine the levels of SDHA, ATP5, ND4, and COX4 protein in NPCs in NC, si-*Gpx1* and si-*Gpx1* + SeNPs groups. **E** Quantitative RT-PCR was used to determine the mRNA levels of genes *Acan* and *Col2a1* in three groups. ($n=4$) **F** Western blotting was used to determine the levels of ACAN and COL2A1 protein in three groups. Statistically significant differences are indicated by * where $P<0.05$ or ** where $P<0.01$ between the indicated group

the SeNP-25 and SeNP-50 groups, respectively, at postoperative 8 weeks. Therefore, these histological results supported the therapeutic potential of SeNPs in treating puncture-induced degeneration in rat lumbar IVDs.

To further investigate the protective effect of SeNPs on the lumbar IVDs, IHC analyses were performed to evaluate the matrix synthesis of ACAN and COL2A1 and the expression levels of GPX1 and IL-1β in the nucleus pulposus tissue. In the IVDD group, the levels of ACAN and COL2A1 decreased markedly, indicating the suppression of matrix sythesis in degenerated nucleus pulposus (Fig. 10A). In comparison, the IHC staining in the SeNP-50 group was strongly postive for both ACAN and COL2A1, suggesting that treatment with 50 ng/mL SeNPs protected the matrix anabolism in punctured IVDs. Quantitative analysis confirmed that the positive aears of ACAN and COL2A1 in the SeNP-50 group at postoperative 8 weeks were 68.1% and 68.1% (Fig. 10B) higher than in the IVDD group, respectively. Furthermore, the IHC staining for GPX1 in the SeNP-50

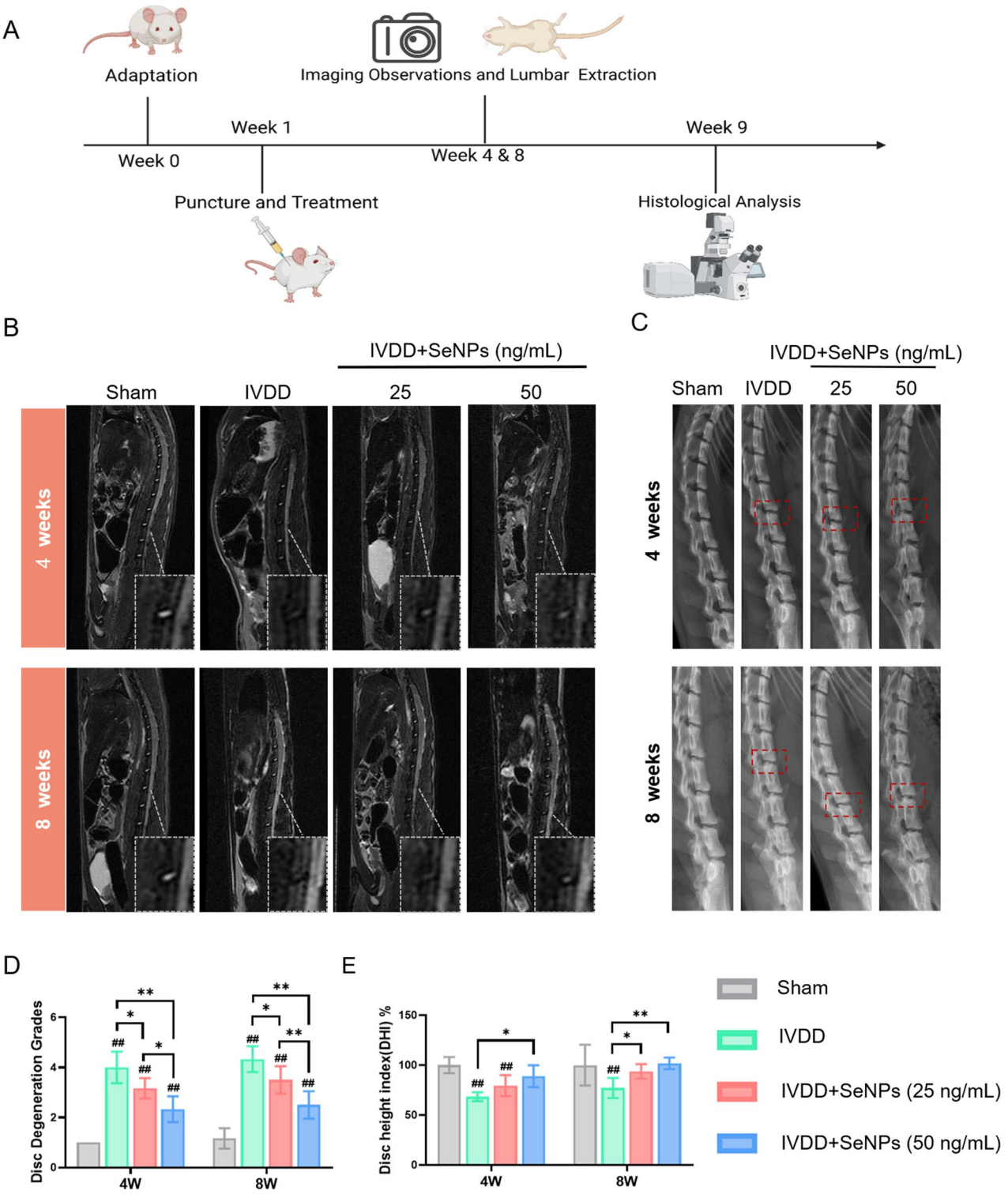

Fig. 8 Establishment of lumbar degenerative model in rats and imaging results of animal experiments. **A** Schematic diagram of the in vivo experiment in rats. **B** Representative MRI images of needing and treated sites in rat lumbar 4 and 8 weeks after surgery. **C** Representative X-ray images of needing and treated sites in rat lumbar 4 and 8 weeks after surgery. **D** Quantification of the optical density values of nucleus pulposus in rats. **E** Quantification of disc height in rats. Statistically significant differences are indicated by # where $P < 0.05$ or ## where $P < 0.01$ compared with the control group; * where $P < 0.05$ or ** where $P < 0.01$ between the indicated group

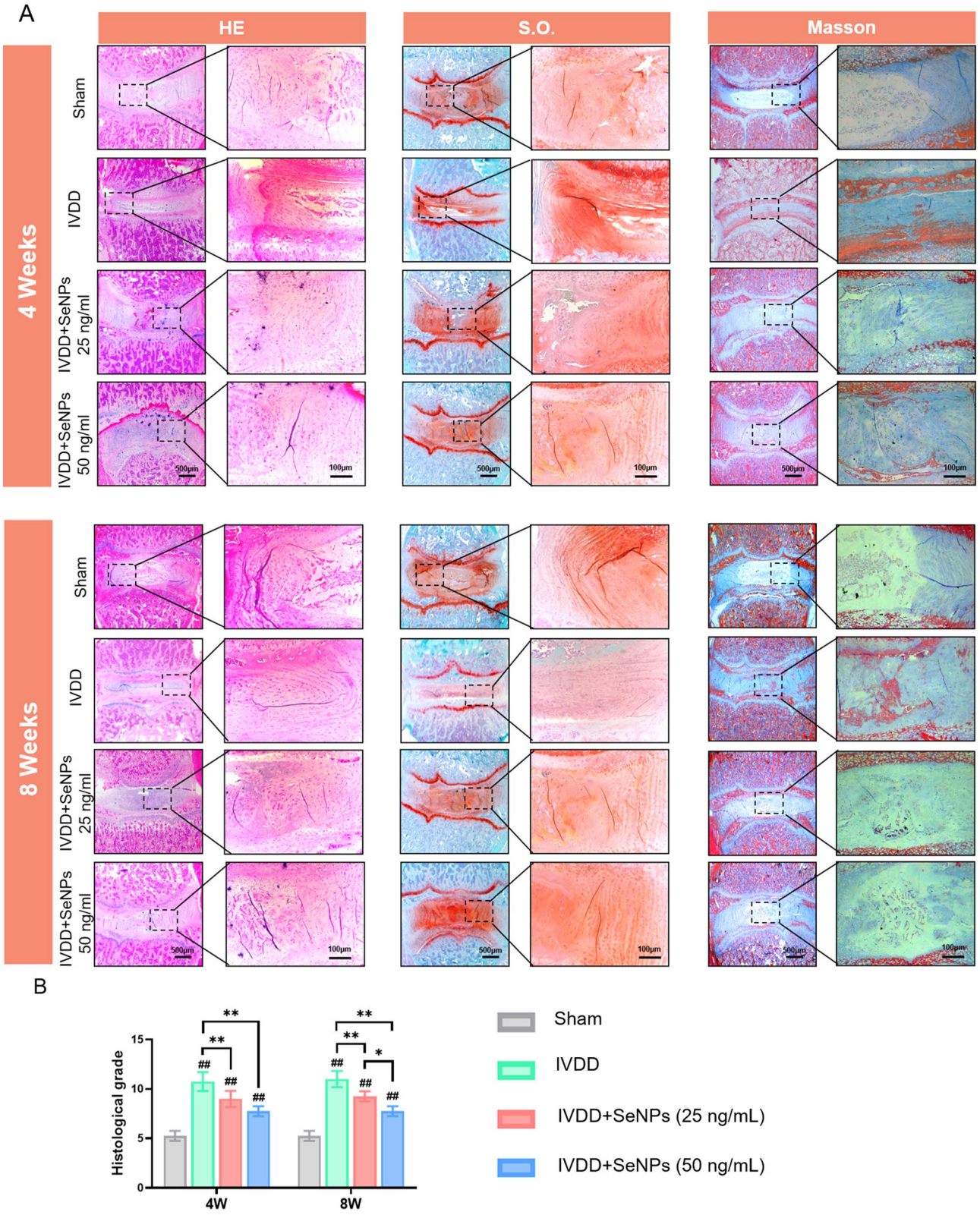

Fig. 9 Histological evaluation of nucleus pulposus tissues in rats at 4 and 8 weeks after treatment. **A** HE, S.O. and Masson staining of needling and treated sites in rat lumbar 4 and 8 weeks after surgery. **B** Quantification of the histological grade scale of HE staining. Statistically significant differences are indicated by # where $P < 0.05$ or ## where $P < 0.01$ compared with the control group; * where $P < 0.05$ or ** where $P < 0.01$ between the indicated group

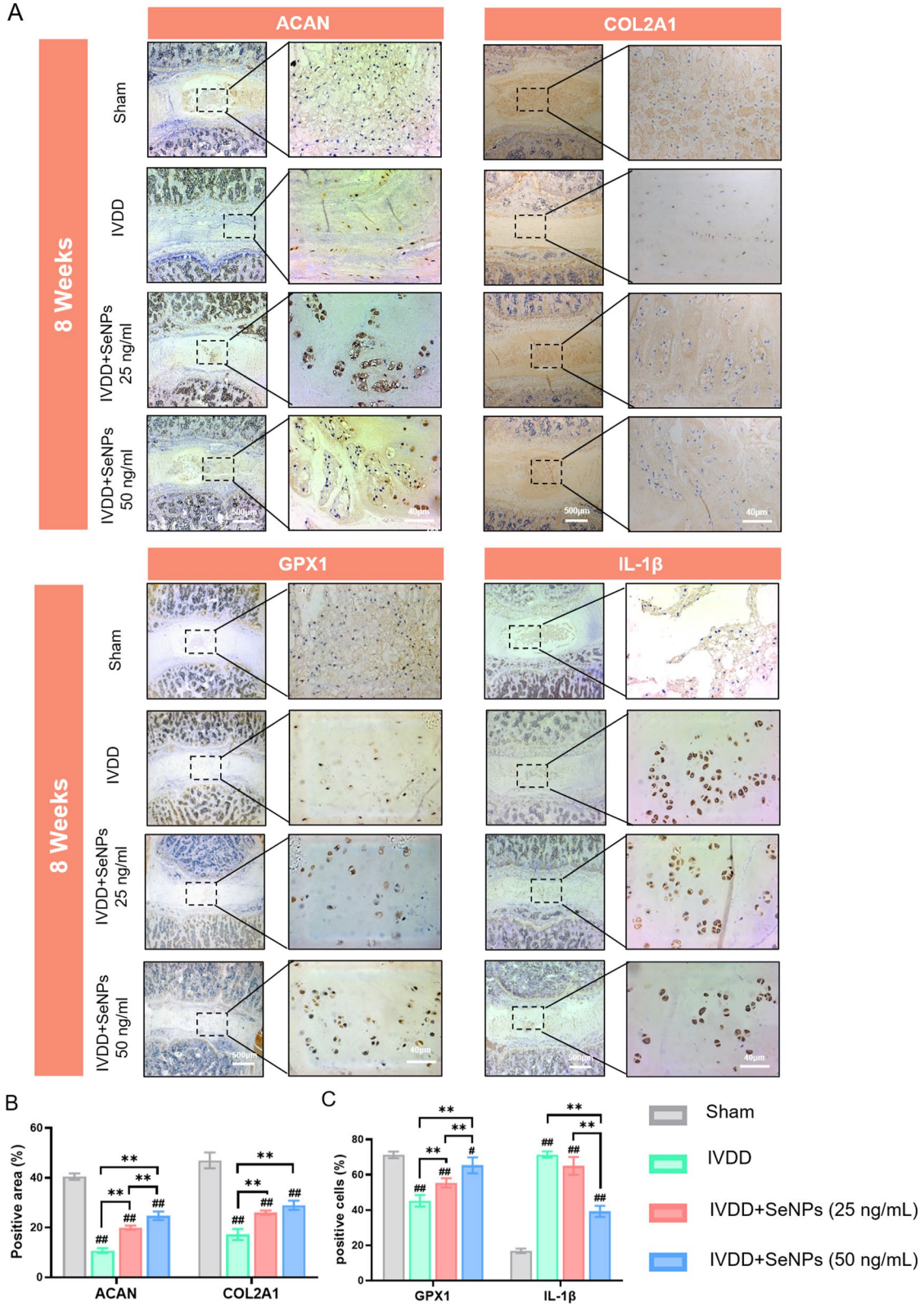

Fig. 10 Immunohistochemical (IHC) stainings of nucleus pulposus tissues in rats at 4 and 8 weeks after treatment. **A** Immunohistochemical staining of protein ACAN, COLIIA1, GPX1 and IL-1β of rats' IVDs at 8 weeks after treatment. **B** Quantification of the percentages of ACAN-positive and COL2A1-positive area in nucleus pulposus tissue. **C** Quantification of the percentages of GPX1-positive and IL-1β-positive cells in nucleus pulposus tissue. Statistically significant differences are indicated by # where $P < 0.05$ or ## where $P < 0.01$ compared with the control group; * where $P < 0.05$ or ** where $P < 0.01$ between the indicated group

group was highly positive compared to the weak yellow color in the IVDD group at postoperative 4 and 8 weeks (Fig. 10A). The percentages of GPX1-positive cells in the SeNP-50 group at postoperative 8 weeks were 44.6% higher than in the IVDD group (Fig. 10C). With regard to the puncture-induced inflammation, treatment with 50 ng/mL SeNPs signficantly decreased expression of inflammatory cytokine IL-1β (Fig. 10C). The percentages of IL-1β-positive cells in the SeNP-50 group were 45.1% lower compared with the IVDD group at postoperative 8 weeks (Fig. 10C). These IHC results demonstrated that SeNPs at the concentration of 50 ng/mL had synergistic effects on ameliorating puncture-induced IVDD by protecting the matrix synthesis capacity, preserving the selenoprotein GPX1 expression, and attenuating the inflammation in degenerated nucleus pulposus.

Discussion

There is a growing body of evidence indicating that selenium, an essential trace element, plays a crucial role in regulating the synthesis and activity of selenoproteins through its incorporation as selenocysteine. This involvement in various physiological processes includes cell viability, mitochondrial function, and ECM remodeling [22]. In a rat model deficient in selenium, impaired skeletal growth and the development of secondary osteoarthritis have been observed, potentially resulting from disrupted ECM metabolism in the growth plate cartilage [23]. Selenium-sensitive protein arginine methyltransferase 5 (PRMT5) may play a role in maintaining cartilage matrix metabolic homeostasis by demethylating and stabilizing the key transcriptional factor SOX9 [24]. In addition, Li et al. observed that dietary selenium deficiency led to significant pathological alterations in the spleen of Yorkshire pigs, attributed to the decreased expression of antioxidant selenoproteins and elevated splenocyte apoptosis via the mitochondrial pathway [25]. Our group recently published findings indicating that selenium-modified bone cement can enhance the regeneration of osteoporotic bone defects in ovariectomized rats by improving intracellular antioxidant functions [17]. In this study, we examined the antioxidant and anti-inflammatory effects of Se-NPCs. Treatment with SeNPs notably reduced intracellular and mitochondrial oxidative stress in NPCs, even in the presence of IL-1β. The strong antioxidant capabilities of SeNPs effectively preserved the integrity of mitochondrial structure and energy metabolism. The anti-inflammatory properties of SeNPs were validated in degenerated IVDs, demonstrating a reduction in IL-1β expression and improvement in matrix degradation.

Pro-inflammatory cytokines are crucial in the advancement of intervertebral disc degeneration, as they induce apoptosis in NPCs and enhance the expression of matrix degradation enzymes [26]. In our research, IL-1β was utilized to simulate the inflammatory milieu in IVDD, revealing that exposure of NPCs to IL-1β significantly inhibited extracellular matrix synthesis, particularly of aggrecan and type II collagen, which are primary components of nucleus pulposus tissue. Biochemical changes that occur in degenerated discs include loss of aggrecan degradation, resulting in decreased osmotic pressure within the disc matrix and loss of hydration, alteration of collagen types and distribution. The induction of cellular senescence in NPCs by IL-1β may lead to decreased ECM synthesis through the promotion of G1 phase cell cycle arrest [27]. IL-1β has been identified as a key regulator of catabolic processes, including ECM degradation and the expression of chemokines such as C-C motif chemokine ligand 2 (CCL2), CCL3, and C-X-C motif chemokine ligand 8 (CXCL8) [28]. Our findings suggest that exposure to IL-1β impairs mitochondrial function in NPCs, as evidenced by reductions in ATP content, mitochondrial depolarization, and down-regulation of respiratory chain factors. Consistently, López-Armada et al. have shown that IL-1β leads to a significant decrease in the key anti-apoptotic factor, B cell leukemia/lymphoma 2 (BCL2), at both the mRNA expression and protein levels in chondrocytes, resulting in increased apoptosis during osteoarthritis pathogenesis [29]. In response to the inflammatory environment induced by IL-1β, NPCs exhibit notable changes in mitochondrial integrity and function, potentially impacting matrix synthesis capacity and matrix degradation enzymes during the IVDD.

In comparison to sodium selenite, SeNPs have demonstrated greater efficacy in mitigating vascular endothelial dysfunction through the reduction of macrophage recruitment and down-regulation of pro-inflammatory factors, indicating the significant potential of SeNPs in the prevention of atherosclerosis [30]. Mechanistically, SeNPs are able to activate the nuclear factor erythroid 2-related factor 2 (NRF2) signaling pathway to enhance the production of antioxidative selenoproteins, thereby inhibiting the expression of ROS-induced inflammatory cytokines in the skin and providing protection against allergic dermatitis [16]. The findings of this study suggest a strong correlation between the protective effects of SeNPs on the matrix synthesis of nucleus pulposus and their potent antioxidant properties. Previous research has also demonstrated that SeNPs can enhance the myogenic differentiation of C2C12 myoblasts, even in the presence of hydrogen peroxide-induced oxidative stress [31]. As a selenium protein, the mitochondrial thioredoxin system is the major H_2O_2 scavenger providing a primary defense against ROS produced by the mitochondrial respiratory chain. It has been verified that aging is associated with significant downregulation of thioredoxin reductase 2 (TXNRD2) expressions in the mammalian heart [32]. TXNRD2 can regulate mitochondrial integrity in the

progression of age-related heart failure [33]. Liu et al. found that TXNRD2 can attenuates early brain injury by inhibition of oxidative stress and endoplasmic reticulum stress after intracerebral hemorrhage in rats [34]. Wang et al. elucidated that selenoprotein K plays a crucial role in skeletal muscle regeneration by mitigating endoplasmic reticulum stress and oxidative stress, with the absence of selenoprotein K hindering the differentiation of myoblasts into myotubes. The findings suggest that selenoprotein K plays a crucial role in the modulation of endoplasmic reticulum stress and cellular redox status [35]. Additionally, selenoprotein W, which is prominently expressed in bone marrow-derived macrophages, has been shown to promote bone resorption by regulating cell-cell fusion necessary for osteoclast maturation [36]. Depletion of selenoprotein W leads to impaired osteoclast formation and bone resorption, likely due to the reliance of these macrophages on oxidative phosphorylation for energy production and the consequential impact of selenoprotein W deletion on the glycolytic metabolism during osteoclastogenesis [37].

Based on the microarray data presented in this study, GPX1 was chosen as a prototypical selenoprotein for investigation of its expression in NPCs. Upon exposure to IL-1β, the expression of GPX1 was markedly reduced at both the transcriptional and protein levels; however, treatment with SeNPs successfully restored its expression. In vivo experiments validated the diminished levels of GPX1 in degenerated nucleus pulposus, whereas local administration of SeNPs reversed this decline and protected the integrity of the nucleus pulposus matrix against degradation. Consistent with our findings, Wang et al. illustrated that SeNPs, upon endocytosis by renal tubular epithelial cells, significantly increased GPX1 levels and hindered kidney fibrosis by suppressing NLRP3 inflammasome activation and Caspase-1 maturation [38]. More importantly, our results suggest that the activation of GPX1 by SeNPs plays a crucial role in enhancing mitochondrial energy metabolism and promoting nucleus pulposus regeneration. The localization of GPX1 within mitochondria resulted in the reduction of ROS levels and enhancement of mitochondrial bioenergetics, encompassing oxygen consumption, ATP production, and lactate dehydrogenase levels [39]. Conversely, the inhibition of *Gpx1* through siRNA negated the beneficial impact of SeNPs on mitochondrial function and matrix equilibrium in NPCs. SeNPs deliver selenium specifically to cells, augmenting both GPX1 expression and antioxidant capacity, thereby protecting mitochondrial function through the regulation of mitophagy and mitigation of endoplasmic reticulum stress in individuals with type 2 diabetes mellitus [40]. On the other hand, prolonged selenium deficiency resulted in hypertension in SD rats, which was linked to a reduction in urine sodium excretion. Further examination of the underlying mechanisms demonstrated that selenium deficiency led to a notable decrease in GPX1 expression, an elevation in oxidative stress, and subsequent activation of the NF-κB signaling pathway in renal proximal tubule cells [41]. Consequently, our forthcoming research will further investigate the impact of SeNPs on endoplasmic reticulum stress and inflammatory response in degenerated IVDs.

The avascular nature of the nucleus pulposus tissue presents challenges for the delivery of SeNPs through oral administration or intraperitoneal injection. This study utilized an in situ injection of SeNPs into degenerated lumbar IVDs following puncture-induced mechanical injury, a method more closely resembling clinical scenarios compared to caudal IVD models [42]. The therapeutic efficacy of SeNPs in promoting nucleus pulposus regeneration was validated through radiographic imaging, histological analysis, and immunohistochemical staining for GPX1. In order to regulate the morphology and distribution of SeNPs, starch has been employed as a natural stabilizing agent for size manipulation. The SeNPs stabilized by starch, possessing notable antioxidant properties, demonstrated significant efficacy in mitigating melamine-induced hepato-renal toxicity in rat models [43]. Furthermore, Ouyang et al. have introduced a novel approach involving hydrogel microbead-based SeNPs, which can be customized with hyaluronic acid and encased in a protective calcium alginate shell to circumvent the acidic conditions of the stomach. The study illustrated that the oral administration of the SeNPs/hydrogel composite elicited in situ selenoprotein synthesis and mitigated inflammation to alleviate symptoms associated with colitis [21]. Moreover, in order to address an inflammatory microenvironment, SeNPs have been incorporated as initiators and nano-fillers into a triple-network dynamic hydrogel. This composite hydrogel has demonstrated an increased capacity for ROS scavenging and notable anti-inflammatory effects by inducing a shift in macrophages towards M2 polarization. As a result, this composite hydrogel shows significant potential for the treatment of inflammatory diseases, such as rheumatoid arthritis, in rat models [44]. Consequently, further research will explore the enhancement of nanoparticle stability and delivery efficacy through the utilization of SeNPs with diverse surface modifications, such as chitosan or cellulose coating [45], and the integration of SeNPs with biocompatible hydrogels or scaffolds [46] will be investigated for the treatment of IVDD.

Conclusion

In summary, we have introduced a straightforward synthesis method for SeNPs that resulted in nanoparticles with consistent size and distribution, as well as desirable biocompatibility. The SeNPs facilitated the production of

ECM components specific to the nucleus pulposus and notably enhanced the mitochondrial activity of NPCs in a dose-dependent manner. Furthermore, in an inflammatory setting, SeNPs effectively mitigated oxidative stress induced by interleukin-1β and inhibited the activity of matrix-degrading enzymes in NPCs. The examination of the underlying mechanism revealed that SeNPs markedly increased the expression of GPX1, a crucial selenoprotein responsible for regulating matrix metabolism and redox homeostasis in NPCs. Following puncture-induced mechanical injury, the local administration of SeNPs mitigated the degeneration of lumbar IVDs in rats, as indicated by an elevation in GPX1 expression, maintenance of nucleus pulposus hydration, and prevention of matrix degradation. This study highlights the potential of SeNPs in enhancing GPX1-mediated mitochondrial function in NPCs, suggesting a promising strategy for the treatment of IVDD.

Materials and methods

Preparation of SeNPs

The synthesis of SeNPs followed a previously established protocol (Fig. 11) [16]. Specifically, 100 mg of gelatin (Sigma-Aldrich, St. Louis, MO, USA) was dissolved in 19 mL of deionized water, to which 6.9 mg of Na_2SeO_3 (Sigma-Aldrich) was added. The resulting mixture was maintained at 4 °C and stirred for 30 min. Subsequently, 56.3 mg of ascorbic acid (Sigma-Aldrich) in 1 mL of deionized water was added dropwise and stirred for an additional 30 min. The synthesized SeNPs underwent dialysis using dialysis membranes (3.5 kDa, Beyotime, Shanghai, China) for 48 h at room temperature to eliminate excess reactants, with the dialysate being replaced every 24 h.

Characterization of SeNPs

The morphological characteristics, distribution, and elemental mapping of SeNPs were observed using TEM (Talos F200X G2, FEI, Hillsboro, OH, USA). Following ultrasonic mixing, the samples were loaded onto copper mesh and analyzed by TEM at an accelerating voltage of 200 kV. The particle size of SeNPs was determined using a Nano-ZS instrument (Malvern Zetasizer Nano ZS90, Malvern, UK) at room temperature. X-ray photoelectron spectroscopy was employed to analyze the structural composition of the SeNPs. The silicon wafer was utilized as a substrate for the deposition of sample drops, which were subsequently dried. The samples were then analyzed using an ESCALAB 250Xi spectrometer (Thermo Scientific K-Alpha, Waltham, MA, USA) featuring an achromatic Al-Kα X-ray source, with the procedure being repeated thrice. FT-IR (Thermo Scientific Nicolet

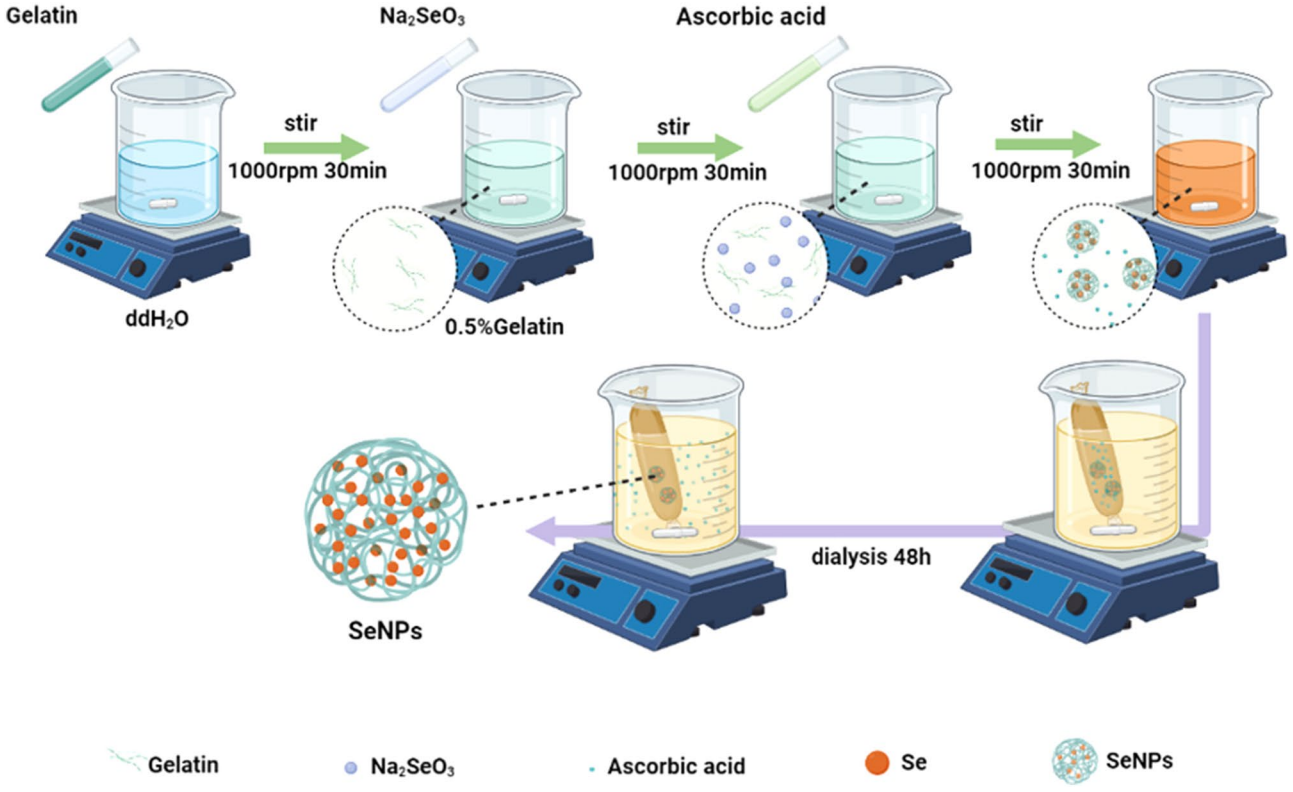

Fig. 11 The synthesis process of SeNPs. Sodium selenite and gelatin were dissolved in deionized water. After dropwisely adding ascorbic acid, sodium selenite is reduced to selenium to form SeNPs. The synthesized SeNPs underwent dialysis remove excess ascorbic acid and other reactants

iS20, Waltham, MA, USA) was employed to characterize the infrared absorption spectrum of SeNPs. An attenuated total refraction (ATR) attachment was positioned in the optical path of the spectrometer to scan the air background. Subsequently, the samples were applied to the crystal surface of the ATR attachment using a dropper, and the infrared spectra of the samples were recorded.

Ingestion rate of SeNPs

The gelatin components in SeNPs were labeled with cy5, and then diluted into concentrations of 25, 50, and 100 ng/mL, respectively, to intervene in NPCs. After 1 day, the cytoskeleton and nuclei were stained with phalloidin (Thermo Fisher Scientific) and 4',6-diamino-2-phenylindole (DAPI, Thermo Fisher Scientific). Images were captured using a Zeiss Axiovert 40CFL microscope and the fluorescence intensity was measured by ImageJ software.

Cell isolation and cell culture

Following euthanasia using CO2, lumbar IVDs were harvested from six-week-old male Sprague-Dawley (SD) rats under aseptic conditions to isolate nucleus pulposus tissues. The isolated nucleus pulposus was then minced and subjected to enzymatic digestion using 0.2% type II collagenase (Thermo Fisher Scientific) at 37 °C for 1.5 h. Subsequently, the digested nucleus pulposus tissues were centrifuged and NPCs were cultured in 175 cm^2 flasks (Costar, Tewksbury, MA, USA) containing Dulbecco's modified Eagle medium (DMEM)/F12 medium (Procell, Wuhan, China) supplemented with 10% fetal bovine serum (FBS, Gibco, Grand Island, NY, USA) and 1% penicillin-streptomycin (Thermo Fisher Scientific) at 37 °C in a humidified atmosphere with 5% CO_2. The culture medium was refreshed every two days, and NPCs were passaged upon reaching 80% confluence using 0.25% trypsin-EDTA (Thermo Fisher Scientific). NPCs at the first passage (P1) were utilized for subsequent experimental procedures.

Live/Dead cell staining assay

NPCs were exposed to SeNPs at varying concentrations (25, 50, and 100 ng/mL) in 12-well plates. Subsequently, the cells were subjected to Live/Dead cell staining (Thermo Fisher Scientific, Waltham, MA, USA) for 15 min, with live cells appearing green and dead cells appearing red. Cell images were then acquired using fluorescence microscopy (Zeiss, Oberkochen, Germany).

Cell proliferation assay

CCK-8 (Beyotime, Haimen, China) was used for cell proliferation assays. NPCs were seeded in a 96-well plate and treated with SeNPs at different concentrations (control, 25 ng/mL, 50 ng/mL and 100 ng/mL). On days 1, 3, and 5, cells were incubated in CCK-8 solution for 1 h at 37 ℃. The optical density (OD) was assessed using a microplate spectrophotometer at 450 nm (BioTek, Winooski, VT, USA).

IL-1β treatment on NPCs

To induce an inflammatory response in vitro, NPCs were treated with 10 ng/mL of recombinant IL-1β (Peprotech, Rocky Hill, NJ, USA) in the culture medium, followed by treatment with SeNPs at different concentrations for three days.

Reverse transcription-quantitative polymerase chain reaction (RT-qPCR)

Total RNA was isolated utilizing TRIzol reagent (Thermo Fisher Scientific), followed by reverse transcription to synthesize complementary DNA using a RevertAid First Strand cDNA Synthesis Kit (Thermo Fisher Scientific) as per the manufacturer's protocol. Subsequently, quantitative RT-PCR amplification of the cDNA was conducted employing an iTap™ Universal SYBR® Green Supermix kit (Bio-Rad, Hercules, CA, USA) in a CFX96™ Real-Time PCR System (Bio-Rad). Gene transcription levels were subsequently quantified, with *Gapdh* (glyceraldehyde 3-phosphate dehydrogenase) serving as the internal control. Relative gene expression was determined using the $2^{-\Delta\Delta Ct}$ method [47], with primer sequences provided in Supplementary Table 1.

Western blotting

NPCs were cultured in 6-well plates and treated with SeNPs. Cells were lysed using RIPA lysis buffer containing phosphatase and protease inhibitors (Thermo Fisher Scientific) to extract protein homogenate. The protein concentration was quantified using the BCA Protein Assay Kit (Beyotime). Equal amounts of protein were subjected to electrophoresis on a 10% sodium dodecyl sulfate-polyarylamide gel (SDS-PAGE) and transferred onto nitrocellulose membranes (Beyotime). Following blocking, the membranes were incubated with primary antibodies (Supplementary Table 2) overnight at 4 °C. The next day, chemiluminescence solution (Thermo Fisher Scientific) was used to visualize protein bands after incubation with secondary antibody (Abcam, Cambridge, MA, USA) for 1 h. Image J software (National Institutes of Health, Bethesda, MD, USA) was utilized for quantitative assessment of protein expression levels based on the gray values of each band, with standardization by β-actin.

Immunofluorescence staining

NPCs were fixed in 4% paraformaldehyde (Sigma-Aldrich) for 10 min, followed by three washes with PBS. Subsequently, samples were treated with 0.1% Triton X-100 (Sigma-Aldrich) for 10 min, blocked with 1% bovine serum for 30 min, and then incubated overnight

at 4 °C with appropriately diluted primary antibodies. The following day, secondary antibodies and phalloidin (Sigma-Aldrich) were applied for 1 h and nuclei were stained with 4',6-diamino-2-phenylindole (DAPI, Thermo Fisher Scientific). Images were captured using a Zeiss Axiovert 40CFL microscope and the fluorescence intensity was measured by ImageJ software.

Intracellular and mitochondrial ROS levels

Intracellular ROS levels were quantified through the use of 2',7'-dichlorofluorescin diacetate (DCFH-DA, Beyotime). Following a 10-min incubation of a 10 μM DCFH-DA solution at 37 ℃ in darkness, fluorescence images were captured utilizing a fluorescence microscope. The resulting fluorescence intensity was subsequently analyzed using ImageJ software. To assess mitochondrial ROS levels, NPCs were exposed to MitoSOX Red (Thermo Fischer Sciences), a specific fluorescent probe capable of detecting superoxides within mitochondria. Following a 10-min incubation with 5 μM MitoSOX Red at 37 ℃, fluorescence images of the mitochondria were visualized using a fluorescence microscope, with fluorescence intensity quantified using ImageJ software.

Fluorescence measurement of mitochondrial morphology

We used MitoTracker Red (Beyotime) to detect the new synthesized mitochondrial. Cells were stained with 200 nM MitoTracker Red for 15 min and DAPI for 1 min before measurement.

Mitochondrial membrane potential (MMP) level

The MMP level was assessed utilizing the Mitochondrial Membrane Potential Assay Kit with JC-1 (Beyotime). NPCs were treated with 0.5 μM JC-1 working solution for 30 min at 37 ℃ in the absence of light, followed by incubation with cold JC-1 staining buffer. Fluorescent images were captured using a fluorescence microscope, and the MMP value was quantified as the ratio of red fluorescence intensity (JC-1 aggregates) to green fluorescence intensity (JC-1 monomers) through the utilization of ImageJ software.

Measurement of GPX enzyme activity

Total GPX activity was determined using the total GPX assay kit (Beyotime) according to the manufacturer's instructions,. The decrease in nicotinamide adenine dinucleotide phosphate measured at 340 nm using a PowerWave XS spectrophotometer (BioTek, Winooski, VT, USA) that was linearly correlated with enzyme activity.

TEM images of Mitochondria in NPCs

The cell sample was initially fixed with a 2.5% glutaraldehyde solution (Sigma-Aldrich) in a phosphate buffer for 4 h. Following a wash with phosphate buffer, the samples underwent treatment with a 1% osmium tetroxide solution (OsO_4, Sigma-Aldrich) in phosphate buffer for 2 h, followed by immersion in ethanol of varying concentrations for 15 min. Subsequently, the samples were subjected to treatment with a mixture of embedding agent and acetone (Sigma-Aldrich) for 3 h. The permeated sample was then embedded and subjected to overnight heating at 70 ℃ to achieve embedding. The embedded samples were sectioned using an ultra-thin microtome and the resulting sections were stained with uranyl acetate and alkaline lead citrate (Sigma-Aldrich) for 10 min each, before being observed using a H-7650 TEM (Hitachi, Tokyo, Japan).

Measurement of intracellular ATP

The intracellular ATP level was quantified using an ATP Assay Kit (Beyotime) following the manufacturer's protocol. NPCs were treated with cell lysate for 5 min at 4 ℃. After centrifugation, ATP detection working solution was added into the supernatant in a microplate. Luminescence was measured using a CentroLB960 instrument (Bertold Technologies, Germany) and normalized to total protein levels determined by the BCA Protein Assay kit (Beyotime).

RNA sequencing for gene expression analysis

Total RNA was extracted utilizing the TRIzol reagent as per the manufacturer's instructions. The concentration of RNA was quantified using a NanoDrop 3000 spectrophotometer (Thermo Fisher Scientific), and RNA quality was assessed with an Agilent 2100 Bioanalyzer (Agilent Technologies, Santa Clara, CA, USA). Library preparation was carried out using the TruSeq Stranded mRNA LT Sample Prep Kit (Illumina, San Diego, CA, USA) following the manufacturer's guidelines. Next-generation sequencing (NGS) and analysis were conducted on the Illumina HiSeq X Ten platform by OE Biotechnology Co. (Shanghai, China) to investigate gene expression patterns at a more granular level for each sample. Mapped reads were generated by aligning against reference genes using the Trimmomatic software HISAT2. GO and KEGG enrichment analysis of differential transcripts were performed using DAVID. Genes were identified as significantly and differentially expressed based on a p-value < 0.05 and FC > 1.5 or < 0.5.

SiRNA transfection

In the context of transient knockdown of *Gpx1* in NPCs, siRNA was procured from Gene Pharma (GenePharma Inc, Shanghai, China) and utilized for transfection of NPCs with either Gpx1-targeting or non-targeting siRNA at a concentration of 100 nM, employing Lipofectamine 3000 (Thermo Fisher Scientific) as per the manufacturer's guidelines. Specifically, 1×10^6 cells were

seeded in each well of 6-well plates and cultured in Opti-MEM medium (Thermo Fisher Scientific) supplemented with the respective siRNA. Following an 8-h transfection period, the culture medium was replaced with fresh growth medium. The specific sequence for *Gpx1* siRNA is detailed in Supplementary Table 1.

Surgical induction of degenearion in rat lumbar IVDs

The animal experiments were conducted following approval by the Ethics Committee of Soochow University (SUDA20230905A03). The rats were categorized into four groups: Sham group, IVDD group, SeNP treatment group at a low concentration (25 ng/mL), and SeNP treatment group at a high concentration (50 ng/mL). Anesthesia was induced in SD rats through intraperitoneal injection of 3% sodium pentobarbital (1.5 mL/kg body weight; Shanghai Merck Co., Ltd., China). Subsequently, a small incision was made on the loin back of the rats after local skin disinfection. Muscle tissue was then separated using microsurgical instruments to expose the L3-4 disc. The lumbar disc was subsequently punctured using a 21 G needle, rotated 360° within the nucleus pulposus, and maintained for 30 s. A volume of 5 μL of SeNPs was then introduced into the nucleus pulposus tissue [48] Postoperatively, the rats received daily intramuscular injections of penicillin (80,000 units) for three days and were housed under controlled environmental conditions including 50–60% humidity, temperatures ranging from 22 to 24 ℃, and a light-dark cycle from 6 AM to 6 PM, with ad libitum access to appropriate diet and water.

Diagnostic imaging

At 4 and 8 weeks following surgery, SD rats were anesthetized and positioned prone for X-ray radiography (250 mA, 50 kV, and 20 ms) using an X-ray Photography System (RADspeed M, Shimadzu, Japan). Disc height loss was assessed by measuring disc height with Image J software and normalizing it to the average height of adjacent vertebrae to calculate the DHI [49].

MRI was conducted using a 1.5 Tesla system (GE Healthcare, Chicago, IL, USA) to acquire T2-weighted images (TR 3500 ms; TE 120 ms; field of view, 200×200 mm; slice thickness, 1.4 mm). The water content in the nucleus pulposus tissue was evaluated by measuring the high signal intensity area in the mid-sagittal T2 image with Image J software [50].

Histology and immunohistochemical staining

The rats were euthanized at 4 and 8 weeks post-surgery, and L3-4 lumbar vertebral specimens were subsequently processed for histological analysis. The specimens were fixed in 10% formalin, decalcified in 10% ethylene diamine tetraacetic acid (EDTA), dehydrated in alcohol, and embedded in paraffin (all from Sigma-Aldrich). Sections of 6 μm thickness were cut using a microtome (Leica Biosystems, Buffalo Grove, IL, USA). Histological evaluation was conducted using hematoxylin and eosin (H&E), Safranin O (S.O.)-fast green, and Masson's trichrome staining techniques (all from Solaibao Technology Co., Ltd, Beijing, China) following the manufacturers' instructions. Histological scoring was performed by two observers (W.H. and X.T.) in a blinded manner [51].

In the process of immunohistochemical staining, paraffin-embedded sections were subjected to dewaxing in xylene and gradient alcohol, followed by a 30-min incubation in 1% hydrogen peroxide (Sigma-Aldrich). Subsequently, the sections were blocked with 1.5% goat serum for 30 min, and then exposed to primary antibodies overnight at 4 ℃. Primary antibodies were used at 1:200 dilution and included rabbit anti-COL2A1 (ab188570, Abcam, Cambridge, UK), anti-Aggrecan (A11691, ABclonal, Wuhan, China), anti-GPX1 (A1110, ABclonal) and anti-IL-1β (A20527, ABclonal). The following day, after rinsing with PBS, the sections were treated with biotinylated goat anti-rabbit secondary antibodies (Abcam) for 30 min and stained with 3,3'-diaminobenzidine solution (DAB, Cell Signaling Technology, Danvers, MA, USA). Finally, the nuclei were counterstained with hematoxylin (Solaibao).

Statistical analysis

For statistical analysis, all experiments were performed in at least three replicates, and data were expressed as mean±standard error of mean (S.E.M). The Student's *t*-test was used to compare two groups, whereas the one-way Analysis of Variance (ANOVA) was performed to compare multiple groups. P values <0.05 (* or $^{\#}$) or <0.01 (** or $^{\#\#}$) were considered statistically significant. All statistical analyses were performed by PRISM 9 (GraphPad Software, San Diego, CA, USA).

Abbreviations

LBP	Low Back Pain
IVDD	Intervertebral Disc Degeneration
IVD	Intervertebral Disc
NPCs	Nucleus Pulposus Cells
ECM	Extracellular Matrix
ROS	Reactive Oxygen Species
ATP	Adenosine Triphosphate
GP	Glutathione Peroxidase
SeNPs	Selenium Nanoparticles
TEM	Transmission Electron Microscopy
FT-IR	Fourier Transform-Infrared Spectrometry
CCK-8	Cell Counting Kit-8
GO	Gene Ontology
KEGG	Kyoto Encyclopedia of Genes and Genomes
siRNA	Small Interfering RNA
NC	Negative Control

Supplementary Information

The online version contains supplementary material available at https://doi.org/10.1186/s12951-024-02890-x.

Supplementary Material 1

Acknowledgements
This study was supported by the National Natural Science Foundation of China (82072476, 82302664), the Natural Science Foundation of Jiangsu Province (BK20220046, BK20230494), Gusu Innovation and Entrepreneur Leading Talents project (ZXL2023204), National High-level Young Talent Program (KS24700124), Jiangsu Specially Appointed Professor Program (SR24700123) and Priority Academic Program Development of Jiangsu Higher Education Institutions (PAPD).

Author contributions
W.H., X.T. and Q.Z. contributed equally to this work. F.H. and Y.X. conceptualized the project and planned, and prepared the work for publication. T.L. provided supports and supervised this study. W.H. performed most experiments and produced all figures and tables. X.T. and Q.Z. performed part of the experiments and helped in data analysis. J.H.L., Y.F.L. and C.Y.J. helped perform the research. H.L. and H.L.Y helped supervised the research and provided reagents. W.H., F.H. and Q.Z. wrote and revised the manuscript. All authors discussed and commented on the manuscript.

Funding
This study was supported by the National Natural Science Foundation of China (82072476, 82302664), the Natural Science Foundation of Jiangsu Province (BK20220046, BK20230494), Gusu Innovation and Entrepreneur Leading Talents project (ZXL2023204), National High-level Young Talent Program (KS24700124), Jiangsu Specially Appointed Professor Program (SR24700123) and Priority Academic Program Development of Jiangsu Higher Education Institutions (PAPD).

Data availability
Data is provided within the manuscript or supplementary information files.

Declarations

Ethics approval and consent to participate
All animal experiments in this study were approved by the Institutional Animal Care and Use Committee of Soochow University.

Consent for publication
All authors agree to be published.

Conflict of interest
The authors declare no conflict of interest.

Author details
[1]Department of Orthopaedics, The First Affiliated Hospital of Soochow University, No. 899 Pinghai Road, Suzhou 215006, Jiangsu, China
[2]Orthopaedic Institute, Suzhou Medical College, Soochow University, No. 178 East Ganjiang Road, Suzhou 215000, Jiangsu, China
[3]Suzhou Medical College of Soochow University, Suzhou 215123, China

Received: 8 June 2024 / Accepted: 1 October 2024
Published online: 18 October 2024

References

1. Francisco V, Pino J, González-Gay M, Lago F, Karppinen J, Tervonen O, Mobasheri A, Gualillo O. Nat Rev Rheumatol. 2022;18:47.
2. Xin J, Wang Y, Zheng Z, Wang S, Na S, Zhang S. Orthop Surg. 2022;14:1271.
3. Pan M, Li Q, Li S, Mao H, Meng B, Zhou F, Yang H. Pain Physician. 2020;23:49.
4. Buckley CT, Hoyland JA, Fujii K, Pandit A, Iatridis JC, Grad S. JOR Spine. 2018;1:1029.
5. Guerrero J, Häckel S, Croft AS, Hoppe S, Albers CE, Gantenbein B. Eur Cell Mater. 2021;41:707.
6. Silagi ES, Shapiro IM, Risbud MV. Matrix Biol. 2018;71–72:368.
7. Mohd Isa IL, Teoh SL, Mohd Nor NH, Mokhtar SA. Int J Mol Sci. 2022;24:208.
8. Czarnocka W, Karpiński S. Free Radic Biol Med. 2018;122:4.
9. Ayer A, Fazakerley DJ, James DE, Stocker R. Free Radic Biol Med. 2022;179:339.
10. Hartman R, Patil P, Tisherman R, St Croix C, Niedernhofer LJ, Robbins PD, Ambrosio F, Van Houten B, Sowa G, Vo N. Eur Cell Mater. 2018;36:171.
11. Napolitano G, Fasciolo G, Venditti P. *Antioxidants* 2021, *10*, 1824.
12. Brigelius-Flohé R, Flohé L. Antioxid Redox Signal. 2020;33:498.
13. Handy DE, Loscalzo J. Free Radic Biol Med. 2022;188:146.
14. Chu Y, Lan RS, Huang R, Feng H, Kumar R, Dayal S, Chan KS, Dai DF. Aging Cell. 2020;19:e13154.
15. Yan J, Guo Y, Fei Y, Zhang R, Han Y, Lu S. Acta Biochim Biophys Sin. 2017;49:110.
16. Xie B, Zeng D, Yang M, Tang Z, He L, Chen T. ACS Nano. 2023;17:14053.
17. Zhou Q, Chen W, Gu C, Liu H, Hu X, Deng L, He W, Xu Y, Zhu X, Yang H, Chen X, He F, Liu T. Regen Biomater. 2023;10:rbad011.
18. Sun K, Wu S, Wang Y, Wan X, Thompson HJ, Zhang J. Food Chem Toxicol. 2013;52:36.
19. Ferro C, Florindo HF, Santos HA. Adv Healthc Mater. 2021;10:e2100598.
20. Chen N, Yao P, Zhang W, Zhang Y, Xin N, Wei H, Zhang T, Zhao C. Crit Rev Food Sci Nutr. 2023;63:12360.
21. Ouyang J, Deng B, Zou B, Li Y, Bu Q, Tian Y, Chen M, Chen W, Kong N, Chen T, Tao W. J Am Chem Soc. 2023;145:12193.
22. Seale LA, Ha HY, Hashimoto AC, Berry MJ. Free Radic Biol Med. 2018;127:182.
23. Ren FL, Guo X, Zhang RJ, Wang Sh J, Zuo H, Zhang ZT, Geng D, Yu Y, Su M. Osteoarthritis Cartilage. 2007;15:1171.
24. Sun M, Hussain S, Hu Y, Yan J, Min Z, Lan X, Guo Y, Zhao Y, Huang H, Feng M, Han Y, Zhang F, Zhu W, Meng L, Li D, Sun J, Lu S. Osteoarthritis Cartilage. 2019;27:932.
25. Li S, Sun W, Zhang K, Zhu J, Jia X, Guo X, Zhao Q, Tang C, Yin J, Zhang J. J Anim Sci Biotechnol. 2021;12:65.
26. Bai X, Yao M, Zhu X, Lian Y, Zhang M. Immunopharmacol Immunotoxicol. 2023;45:433.
27. Huang X, Chen C, Chen Y, Xu J, Liu L. Bioengineered. 2022;13:13849.
28. Phillips KL, Cullen K, Chiverton N, Michael AL, Cole AA, Breakwell LM, Haddock G, Bunning RA, Cross AK, Le Maitre CL. Osteoarthritis Cartilage. 2015;23:1165.
29. López-Armada MJ, Caramés B, Martín MA, Cillero-Pastor B, Lires-Dean M, Fuentes-Boquete I, Arenas J, Blanco FJ. Osteoarthritis Cartilage. 2006;14:1011.
30. Xiao J, Li N, Xiao S, Wu Y, Liu H. Int J Mol Sci. 2021;22:11612.
31. Lee SC, Lee NH, Patel KD, Jun SK, Park JH, Knowles JC, Kim HW, Lee HH, Lee JH. *Antioxidants* 2021, *10*,1727.
32. Yoshioka J. J Am Heart Assoc. 2015;4:7.
33. Rohrbach S, Gruenler S, Teschner M, Holtz J. Am J Physiol Regul Integr Comp Physiol. 2006;291:4.
34. Liu X, Hong E, Xie J, Li J, Ding B, Chen Y, Xia Z, Jiang W, Lv H, Yang B, Chen Y. Neuroscience. 2024;545:158.
35. Wang S, Zhao X, Liu Q, Wang Y, Li S, Xu S. Redox Biol. 2022;50:102255.
36. Kim H, Lee K, Kim JM, Kim MY, Kim JR, Lee HW, Chung YW, Shin HI, Kim T, Park ES, Rho J, Lee SH, Kim N, Lee SY, Choi Y, Jeong D. Nat Commun. 2021;12:2258.
37. Misra S, Lee TJ, Sebastian A, McGuigan J, Liao C, Koo I, Patterson AD, Rossi RM, Hall MA, Albert I, Prabhu KS. Redox Biol. 2023;59:102571.
38. Wang S, Chen Y, Han S, Liu Y, Gao J, Huang Y, Sun W, Wang J, Wang C, Zhao J. *Theranostics* 2022, *12*, 3882.
39. Aashique M, Roy A, Diamond A, Bera S. J Cell Biochem. 2019;120:3393.
40. Huang Q, Liu Z, Yang Y, Yang Y, Huang T, Hong Y, Zhang J, Chen Q, Zhao T, Xiao Z, Gong X, Jiang Y, Peng J, Nan Y, Ai K. Adv Sci. 2023;10:e2300880.
41. Lei L, Zhang F, Huang J, Yang X, Zhou X, Yan H, Chen C, Zheng S, Si L, Jose PA, Zeng C, Yang J. Free Radic Biol Med. 2023;200:59.
42. Wawrose RA, Couch BK, Dombrowski M, Chen SR, Oyekan A, Dong Q, Wang D, Zhou C, Chen J, Modali K, Johnson M, Sedor-Schiffhauer Z, Hitchens TK, Jin T, Bell KM, Lee JY, Sowa GA, Vo NV. JOR Spine. 2022;5:e1202.
43. Ahmed ZSO, Galal MK, Drweesh EA, Abou-El-Sherbini KS, Elzahany EAM, Elnagar MM, Yasin NAE. Int J Biol Macromol. 2021;191:792.
44. Wang S, Liu Y, Sun Q, Zeng B, Liu C, Gong L, Wu H, Chen L, Jin M, Guo J, Gao Z, Huang W. Adv Sci. 2023;10:e2303167.
45. Chen Y, Stoll S, Sun H, Liu X, Liu W, Leng X. Carbohydr Polym. 2022;278:118859.
46. Muchová J, Hearnden V, Michlovská L, Vištejnová L, Zavaďáková A, Šmerková K, Kočiová S, Adam V, Kopel P, Vojtová L. J Nanobiotechnol. 2021;19:103.
47. Noonan KE, Beck C, Holzmayer TA, Chin JE, Wunder JS, Andrulis IL, Gazdar AF, Willman CL, Griffith B, Von Hoff DD, Roninson IB. Proc Natl Acad Sci U S A. 1990;87:7160.
48. Zhou T, Yang X, Chen Z, Yang Y, Wang X, Cao X, Chen C, Han C, Tian H, Qin A, Fu J, Zhao J. Adv Sci 2022, 9, e2105466.

49. Masuda K, Aota Y, Muehleman C, Imai Y, Okuma M, Thonar EJ, Andersson GB, An HS. Spine. 2005;30:5.
50. Pfirrmann CW, Metzdorf A, Zanetti M, Hodler J, Boos N. Spine. 2001;26:1873.
51. Lai A, Gansau J, Gullbrand SE, Crowley J, Cunha C, Dudli S, Engiles JB, Fusellier M, Goncalves RM, Nakashima D, Okewunmi J, Pelletier M, Presciutti SM, Schol J, Takeoka Y, Yang S, Yurube T, Zhang Y, Iatridis JC. JOR Spine. 2021;4:e1150.

Publisher's note